A refined diffuse cohesive approach for the failure analysis in quasibrittle materials—part I: Theoretical formulation and numerical calibration

FFEMS-8224_R2

A refined diffuse cohesive approach for the failure analysis in quasi-brittle materials – Part I: theoretical formulation and numerical calibration

Umberto De Maio[1], Fabrizio Greco[1], Lorenzo Leonetti[2], Raimondo Luciano[3], Paolo Nevone Blasi[1], Sabrina Vantadori[2]

[1] Department of Civil Engineering, University of Calabria, Rende, Italy

[2] Department of Engineering and Architecture, University of Parma, Parma, Italy

[3] Department of Engineering, Parthenope University of Naples, Naples, Italy

Abstract

In this work, a refined inter-element diffuse fracture theoretical model, based on a cohesive finite element approach, is proposed for concrete and other quasi-brittle materials. This model takes advantage of a novel micromechanics-based calibration technique for reducing the artificial compliance associated with the adopted intrinsic formulation. By means of this technique, the required values for the elastic stiffness parameters to obtain nearly invisible cohesive interfaces are provided. Furthermore, the mesh-induced toughening effect, essentially related to the artificial crack tortuosity caused by the different orientations of the inter-element cohesive interfaces, is numerically investigated by performing comparisons with an additional fracture model, newly introduced for the purpose of numerical validation. These comparisons are presented to assess the reliability and the numerical accuracy of the proposed fracture approach.

KEYWORDS

Crack propagation, inter-element fracture, embedded interface model, cohesive finite elements, micromechanics-based techniques, quasi-brittle materials.

Nomenclature: $\bar{\boldsymbol{C}}$, homogenized moduli tensor, $\bar{\boldsymbol{C}}^{(\mathrm{UT})},\bar{\boldsymbol{C}}^{(\mathrm{G})},\bar{\boldsymbol{C}}^{(\mathrm{LD})}$, homogenized moduli tensor for uniform traction (UT), general (G) and linear displacement (LD) boundary conditions; $\bar{\boldsymbol{C}}^{\mathrm{iso}}$, isotropic moduli tensor closest to $\bar{\boldsymbol{C}}$; $\langle\bar{\boldsymbol{C}}\rangle_{\phi}$, angularly averaged homogenized moduli tensor; CDIM, controlled diffuse interface model; d, scalar damage function; DIM, diffuse interface model; E, Young's modulus of the bulk; $\bar{E}$, overall Young's modulus; e_E, percentage variation of the overall Young's modulus; e_C, percentage deviation of the homogenized moduli; G, tangential modulus of the bulk; $\bar{G}$, overall tangential modulus; $\bar{G}_{2\mathrm{D}}$, homogenized planar shear modulus; $G_{\mathrm{I}},G_{\mathrm{II}}$, modal components of the energy release rate; $G_{\mathrm{Ic}},G_{\mathrm{IIc}}$, mode-I and mode-II fracture energies; i_a, anisotropy index; i_c, compliance index; $\boldsymbol{K}$, second-order secant interfacial constitutive tensor; $\boldsymbol{K}_0$, second-order elastic interfacial constitutive tensor; K_n,K_s, normal and tangential interfacial cohesive stiffness parameters; K_n^0,K_s^0, normal and tangential interfacial elastic stiffness parameters; $\bar{K}_{2\mathrm{D}}$, homogenized planar bulk modulus; L_{mesh}, mesh size; L_{RVE}, RVE size; $\boldsymbol{Q}$, proper orthogonal transformation tensor; R_E, reduction of the Young's modulus; R_G, reduction of the tangential modulus; R_ν, reduction of the Poisson's ratio; RVE, representative volume element; SIM, single interface model; $\boldsymbol{t}_{\mathrm{coh}}$, cohesive traction vector; $t_n^{\mathrm{coh}},t_s^{\mathrm{coh}}$, normal and tangential components of the cohesive traction vector; $\boldsymbol{u}$, displacement jump between the crack faces; α, dimensionless cohesive softening parameter; β, tangential-to-normal displacement jump ratio; γ, mesh topology factor; Γ_d^h, internal mesh boundaries; δ_m, mixed-mode displacement jump; δ_m^0, effective displacement jump at damage onset; δ_m^f, effective displacement jump at total decohesion; $\delta_m^{\max}$, maximum effective displacement jump during deformation history; δ_n,δ_s, normal and tangential components of the displacement jump; δ_n^0,δ_s^0, normal and tangential

displacement jumps at damage onset in pure mode-I and mode-II, respectively; $\bar{\boldsymbol{\varepsilon}}$, prescribed macro-strain tensor; κ, dimensionless interfacial normal stiffness; ν, Poisson's ratio of the bulk; $\bar{\nu}$, overall Poisson's ratio; ξ, tangential-to-normal stiffness ratio of the interface; ρ, dimensionless RVE size; σ, normal stress component; $\bar{\boldsymbol{\sigma}}$, macro-stress tensor; $\sigma_{\max}$, normal critical interface stress; τ, shear stress component; $\tau_{\max}$, tangential critical interface stress; Φ_d, dissipated fracture energy.

1. INTRODUCTION

Several construction materials exhibit a quasi-brittle mechanical response at common spatial scales (i.e. laboratory and building scales), associated with the development of a fracture process zone (FPZ) before the occurrence of strain localization. In detail, their fracture behavior is characterized by a gradual transition from an initial diffuse damaged state, in which several micro-cracks grow and interact with each other, to a complete localized damaged state, leading to the nucleation and subsequent propagation of macroscopic cracks. With the aim of analyzing crack propagation in such materials, both discrete and smeared crack models have been widely used in the literature[1].

In discrete fracture modeling, both linear and nonlinear fracture mechanics models have been used in the literature for crack analysis of concrete and other quasi-brittle materials. Since Linear Elastic Fracture Mechanics (LEFM) models assume that the energy dissipation is confined within a vanishing region located in front of a macroscopic crack tip, they have been successfully applied to large concrete structures like dams[2]. Another well-known application of LEFM for concrete structures is the prediction of the pull-out test, as confirmed by some recent numerical works (see, for instance, Piccinin et al.[3]). In more general situations, NLFM models are mandatory to capture the typical size-effects in concrete[4]. As a matter of fact, the real FPZ extension cannot be neglected in common small- and medium-sized structures. Among all the NLFM models, cohesive zone models (CZMs) are the most used for concrete-like materials[5].

Within a finite element setting, two main strategies can be found in the literature for simulating cohesive fracture, i.e. inter-element and intra-element models. In the first approach, cohesive cracks are constrained to be extended between the finite elements, whereas in the latter, cohesive cracks propagate across them.

Inter-element crack propagation is usually accounted for by using cohesive interface elements of the so-called intrinsic type, inserted prior to the simulation along predefined crack locations. Thus, such a modeling has been extensively used in the presence of a priori-known crack paths, like in debonding problems usually experienced in composite materials[6-13]. On the contrary, in the case of unknown crack patterns, interface elements of the so-called extrinsic type are inserted during the simulation in an adaptive manner, after introducing specific insertion criteria into the model[14,15]. Such a modeling usually requires highly time-consuming remeshing operations, which can be reduced if local remeshing strategies are developed (see, for instance, Kuutti and Kolari[16]). Furthermore, due to remapping of the stresses and strains (and, eventually, of the damage variables), remeshing may cause thermodynamically inadmissible healing of previously cracked regions, posing severe uniqueness problems in the occurrence of crack branching.

Intra-element fracture approaches have been widely used to simulate crack initiation and propagation along unknown crack paths (or patterns) without requiring any remeshing. According to these approaches, the propagating discontinuities are embedded by introducing a kinematic enrichment either at the element level, as in the strong discontinuity approach (SDA)[17], or at the node level (equipped with additional degrees of freedom), as in the partition of unity finite element method (PUFEM)[18], the extended finite element method (XFEM)[19], the phantom node method (PNM)[20], and the cohesive segment method (CSM)[21].

In contrast to discrete fracture models, in smeared crack approaches the fracture energy is distributed over the continuum[22-24]. As is well known, the strain softening injected in the constitutive response locally leads to a change in the character of the governing partial differential equations. This change inevitably leads to an ill-posed boundary value problem (BVP), thus rendering such approaches susceptible to localization instabilities (and spurious mesh sensitivities if these continua are approximated by finite element models)[25,26]. These theoretical and numerical difficulties have been tackled in the literature by introducing into the material model some localization limiters, assuring the energy dissipation to be confined within a band across the ideal discontinuity line. Different localization limiters have been proposed in the literature, such as crack band models[27], fracture energy-based regularization techniques[28], and the more rigorous nonlocal continuum models, including integral[29], strain gradient[30], and micropolar[31-32] models.

It is recognized that regularized smeared crack models are reliable in predicting the load-carrying capacity of quasi-brittle materials in the strain softening regimes without sensible mesh-dependency issues, but they are not able to capture crack initiation, growth, coalescence and branching, because their essential features are inevitably lost in the smoothing process. Therefore, they are not suitable for crack analyses in concrete-like structures, unless special post-processing methods are introduced to extract crack geometries[33].

An interesting method able to overcome the main limitations of both discrete and smeared crack approaches is the cohesive finite element method, based on an inter-element fracture representation, by which multiple cracking in quasi-brittle materials is handled in a natural way. The advantages of this approach are twofold. Firstly, it is an efficient and readily implementable approach for predicting crack initiation and propagation along non-prescribed paths within a standard displacement-type finite element setting, without injecting any enriched kinematics into the solid elements, unlike intra-element techniques. Secondly, it preserves the discrete nature of fracture processes, resulting in a very good capability of capturing the real crack patterns. The cohesive finite element method takes inspiration from a series of seminal works about the simulation of intergranular fracture in polycrystalline materials[34-36], in which interface elements of the intrinsic type were inserted at the grain boundaries prior to the simulation. In Xu and Needleman[37], the cohesive approach was further extended to model crack propagation along arbitrary paths in homogeneous brittle elastic media, by inserting interface elements along all the mesh boundaries. However, such an approach, being the first application of the cohesive finite element method in the literature, inevitably led to mesh dependency issues, in terms of lack of spatial convergence for arbitrary crack paths (see Papoulia et al.[38] for a discussion).

The mesh dependency of the cohesive finite element method is experienced even in the elastic range, mainly due to the artificial compliance increase associated with the insertion of springs with finite stiffness between all the bulk finite elements. Such a dependency may be alleviated by calibrating the initial cohesive stiffness parameters as functions of the adopted mesh size, as suggested by many authors[39-43,7]. Nevertheless, to the best knowledge of the authors, the cohesive finite element method could not be fully exploited because the reliability of the associated numerical results is negatively affected by the absence of a sound strategy for controlling and/or reducing such mesh dependency effects under general boundary and loading conditions. To this end, in this paper a refined version of the inter-element cohesive methodology recently introduced by some of the authors[44], is presented under the name of diffuse interface model (DIM). Unlike the previously proposed approach, the present model is capable to handle mesh-dependency issues in the elastic range in a rigorous manner.

The main aspect of novelty with respect to [44] is the adoption of a new micromechanics-based calibration approach for the stiffness parameters of the cohesive interfaces. This approach, whose aim is to control the above-discussed mesh-induced artificial compliance, results from the synergistic application of fracture mechanics concepts and the well-established homogenization techniques (see, for instance, [45-51] to have an overview about the latter ones). The adopted numerical homogenization scheme has allowed the analytical results found in [41,43] to be extended to more general mesh and loading configurations.

Furthermore, the DIM approach is also validated in the nonlinear range, by investigating the toughening effect induced by the mesh, which is unavoidable and essentially related to the artificial crack tortuosity. To this end, a novel fracture model is introduced for the purpose of comparison, obtained by adjusting the position of the mesh nodes, such that the inter-element boundaries are forced to lie along a predefined main crack path. This reference model is used to assess the reliability and the accuracy of the DIM approach.

2. THEORETICAL BACKGROUND

In the section, the theoretical formulation of the adopted cohesive finite element method will be briefly presented, with reference to the special case of planar elasticity. Subsequently, the mesh-induced elastic compliance effects will be investigated. Finally, a novel calibration criterion for the initial cohesive stiffness parameters will be presented, relying on a rigorous numerical micromechanical approach.

2.1. The cohesive finite element method: variational formulation

The description of the cohesive finite element approach is split in two steps. In the first one, the variational formulation for a fractured continuum is reported by considering an a priori-known crack path. In the second one, this formulation is extended to unknown crack locations. Both variational formulations are presented in the following, assuming, without loss of generality, small displacements and negligible inertial forces.

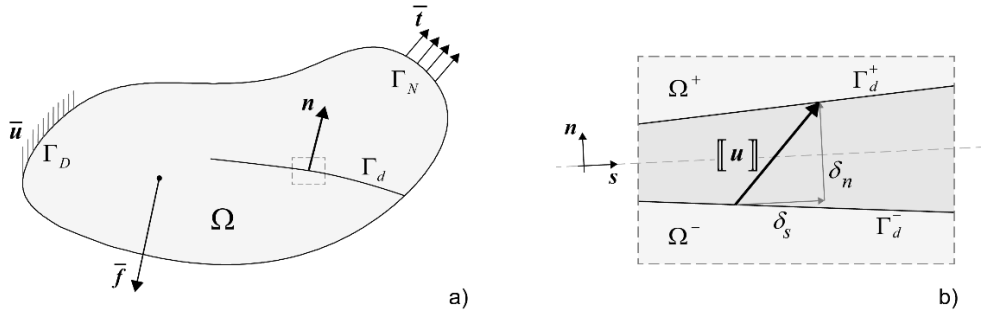

Fig. 1. Equilibrium problem for a 2D fractured body: (a) schematic representation of the body; (b) representation of the crack and related notations.

The first variational formulation refers to the problem of the fractured body depicted in Fig. 1a, containing a single discontinuity line, representing an existing crack lying on a path which is known a priori. Let Ω be the region occupied by the body, defined as a bounded open set in R^2. Its boundary Γ is supposed to be Lipschitz continuous and divided into the subsets Γ_N and Γ_D, where Neumann and Dirichlet boundary conditions are imposed, respectively, such that $\Gamma_N \cap \Gamma_D = \varnothing$ and the measure of Γ_D is greater than zero to avoid arbitrary rigid-body motions. Such a fractured body is subjected to a system of body forces $\bar{\boldsymbol{f}}$ in Ω, and of surface forces $\bar{\boldsymbol{t}}$ on Γ_N, whereas a prescribed displacement $\bar{\boldsymbol{u}}$ is applied on Γ_D. The embedded discontinuity line, denoted by Γ_d, is the union of the two (positive and negative) crack faces, referred to as Γ_d^+ and Γ_d^- (see Fig. 1b). The adopted cohesive formulation implies that the cohesive tractions $\boldsymbol{t}_{\text{coh}}^+$ and $\boldsymbol{t}_{\text{coh}}^-$, acting respectively on the positive and negative sides of the given discontinuity, are self-balanced.

The material response of the bulk phase is assumed to be linearly elastic and isotropic, so that the only nonlinearity source is the constitutive behavior of the cohesive crack, which can be expressed by a traction-separation law of the kind $\boldsymbol{t}_{\text{coh}} = \boldsymbol{K}\left(\ \boldsymbol{u}\ \right)\boldsymbol{u}$, relating the cohesive traction $\boldsymbol{t}_{\text{coh}}^- = \boldsymbol{t}_{\text{coh}}$ to the displacement jump between the crack faces, defined as $\boldsymbol{u} = \boldsymbol{u}^+ - \boldsymbol{u}^-$, via the second-order constitutive tensor $\boldsymbol{K}$. In the absence of direct cross coupling between normal and tangential modes, such a tensor can be expressed in terms of the normal and tangential cohesive stiffness parameters, denoted by K_n and K_s, respectively:

$$\boldsymbol{K}\left(\ \boldsymbol{u}\ \right) = K_n\left(\ \boldsymbol{u}\ \right)\boldsymbol{n}\otimes\boldsymbol{n} + K_s\left(\ \boldsymbol{u}\ \right)\left(\boldsymbol{I} - \boldsymbol{n}\otimes\boldsymbol{n}\right). \tag{1}$$

Such a cohesive interface behaves as a bed of nonlinear springs acting on the normal and tangential components of the displacement jump, i.e. $\delta_n = \boldsymbol{u}\cdot\boldsymbol{n}$ and $\delta_s = \boldsymbol{u}\cdot\boldsymbol{s}$, where $\boldsymbol{n}$ and $\boldsymbol{s}$ are the unit normal and tangent vectors to Γ_d^-, respectively (see Fig. 1b).

By means of standard variational arguments, the quasi-static equilibrium problem of such a body can be formulated as a nonlinear BVP expressed in the following weak form: find $\boldsymbol{u} \in U$ such that:

$$\int_{\Omega\setminus\Gamma_d} \boldsymbol{C}\,\nabla_s\boldsymbol{u}:(\nabla_s\boldsymbol{v})\,\mathrm{d}\Omega+\int_{\Gamma_d}\boldsymbol{K}(\,\boldsymbol{u}\,)\,\boldsymbol{u}\cdot\boldsymbol{v}\;\;\mathrm{d}\Gamma=\int_{\Omega\setminus\Gamma_d}\bar{\boldsymbol{f}}\cdot\boldsymbol{v}\,\mathrm{d}\Omega+\int_{\Gamma_N}\bar{\boldsymbol{t}}\cdot\boldsymbol{v}\,\mathrm{d}\Gamma\qquad\forall\boldsymbol{v}\in V\,,\tag{2}$$

where $\boldsymbol{C}$ is the elasticity tensor, the double-dot symbol denotes the inner product of two second-order tensors, ∇_s is the symmetric part of the gradient operator, $\boldsymbol{u}$ and $\boldsymbol{v}$ are the (unknown) displacement field and the arbitrary virtual displacement field, respectively, belonging to the following sets:

$$\begin{aligned} U&=\left\{\boldsymbol{u}\,\text{such that}\,\boldsymbol{u}\in H^1(\Omega\setminus\Gamma_d)\;\text{and}\;\boldsymbol{u}\big|_{\Gamma_D}=\bar{\boldsymbol{u}}\right\}\\ V&=\left\{\boldsymbol{v}\,\text{such that}\,\boldsymbol{v}\in H^1(\Omega\setminus\Gamma_d)\;\text{and}\;\boldsymbol{v}\big|_{\Gamma_D}=\boldsymbol{0}\right\}\end{aligned}\,,\tag{3}$$

where $H^1(\Omega\setminus\Gamma_d)$ is the Sobolev space of degree one defined over the bulk phase, and the backslash symbol stands for the set difference. It is useful to observe that the second term appearing on the left-hand side of Eq. (2) represents the virtual work of the cohesive tractions over the discontinuity line.

The second variational formulation discussed here, upon which the cohesive finite element method is based, is written for a spatial discretization of the given body. To this end, a planar tessellation of Ω is considered, $\Omega^h\subset R^2$, which is not constrained by the presence of the existing discontinuity line Γ_d. It follows that Γ_d, representing the exact crack path, must be approximated as a set of cohesive segments Γ_d^h, restricted to lie along the nearest inter-element boundaries (see Fig. 2a).

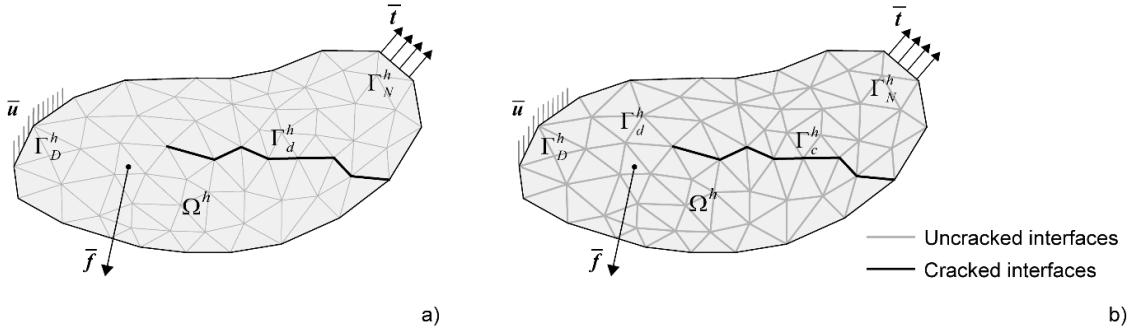

Fig. 2. Schematic representation of the BVP for a cracked discretized body with: (a) cohesive interfaces approximating the exact crack path; (b) cohesive interfaces approximating all the potential crack paths.

If the crack path is not known a priori, all the internal mesh boundaries can be regarded as discontinuity lines, and replaced by zero-thickness interfaces Γ_d^h inserted a priori between all the adjacent bulk elements of Ω^h (see Fig. 2b). The associated BVP expressed in weak form reads as: find $\boldsymbol{u}^h\in U^h$ such that:

$$\int_{\Omega^h\setminus\Gamma_d^h}\boldsymbol{C}\,\nabla_s\boldsymbol{u}^h:(\nabla_s\boldsymbol{v}^h)\,\mathrm{d}\Omega+\int_{\Gamma_d^h}\boldsymbol{K}(\boldsymbol{u}^h)\boldsymbol{u}^h\cdot\boldsymbol{v}^h\,\mathrm{d}\Gamma=\int_{\Omega^h\setminus\Gamma_d^h}\bar{\boldsymbol{f}}\cdot\boldsymbol{v}^h\,\mathrm{d}\Omega+\int_{\Gamma_N^h}\bar{\boldsymbol{t}}\cdot\boldsymbol{v}^h\,\mathrm{d}\Gamma\qquad\forall\boldsymbol{v}^h\in V^h\,,\tag{4}$$

where the superscript h refers to the discretized counterparts of the quantities appearing in Eq. (2). In this formulation, Ω^h and Γ_d^h have the following definitions:

$$\Omega^h = \bigcup_{e=1}^{n_e} \bar{\Omega}_e^h; \qquad \Gamma_d^h = \left[\bigcup_{e=1}^{n_e} \Gamma_e^h \right] \setminus \Gamma^h, \tag{5}$$

where Ω_e^h is a generic finite element with boundary Γ_e^h, $\bar{\Omega}_e^h$ represents its closure, i.e. $\bar{\Omega}_e^h = \Omega_e^h \cup \Gamma_e^h$, and the union operator acts over all the n_e finite elements of the given discretization.

It is worth noting that, in this case, Γ_d^h is no longer coincident with the actual cracks, but represents the set of all potential lines for crack propagation. The set of actual cracks, characterized by a nonlinear behavior, is denoted by $\Gamma_c^h \subset \Gamma_d^h$. As a matter of fact, the remaining (uncracked) interfaces $\Gamma_d^h \setminus \Gamma_c^h$ behave as linear elastic springs, whose initial stiffness components $K_n^0 = K_n\left(\llbracket \boldsymbol{u}^h \rrbracket = \mathbf{0}\right)$ and $K_s^0 = K_s\left(\llbracket \boldsymbol{u}^h \rrbracket = \mathbf{0}\right)$ play the role of penalty parameters to enforce the inter-element continuity, without having a physical meaning.

2.2. Investigation of the mesh-induced compliance effects

For quasi-brittle materials, where damage is usually localized around existing macro-cracks, only a small percentage of the cohesive interfaces may be regarded as active, whereas the remaining are worthless. In addition, due to the adoption of an intrinsic cohesive model, these unnecessary interfaces negatively affect the mechanical response of the body by seriously reducing its overall material stiffness. As a matter of fact, since the initial cohesive stiffness must be kept finite, the insertion of the interface elements along all the internal mesh boundaries inevitably leads to an artificial reduction in stiffness even at the elastic stage.

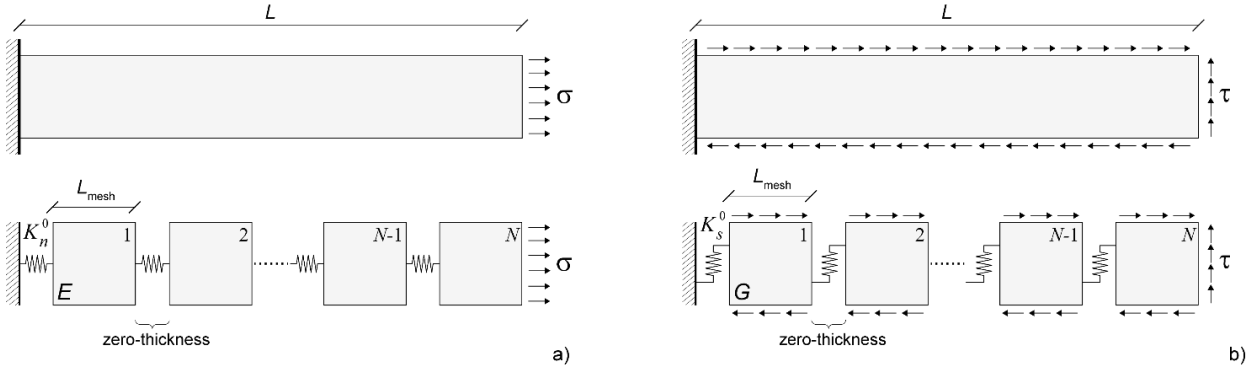

Fig. 3. Mesh-induced artificial compliance in a rectangular plate: (a) overall elastic behavior in the normal direction; (b) overall elastic behavior in the tangential direction.

The longitudinal stiffness reduction induced by the presence of diffuse cohesive interfaces can be analyzed by considering a simple specimen, already used by Klein et al.[39], consisting in a rectangular plate subjected to a uniaxial tensile stress σ (see Fig. 3a). This plate, whose length is denoted by L, is discretized into N equally sized quadrilateral elements with linearly elastic behavior and N zero-thickness interface elements. The length of each bulk element, denoted by L_{mesh}, is equal to L/N. Moreover, E and K_n^0 denote the Young's modulus of the bulk material and the initial normal stiffness of the cohesive interface, respectively. The total elongations of the bulk and interface elements are $\Delta L_b = L\sigma/E$ and $\Delta L_c = N\sigma/K_n^0$, respectively.

It follows that the uniaxial strain ε of the plate can be computed as $\left(\Delta L_b + \Delta L_c\right)/L = \left(L\sigma/E + N\sigma/K_n^0\right)/L$, leading to the following expression for the overall elastic modulus, $\bar{E} = \sigma/\varepsilon = 1/\left(1/E + N/(LK_n^0)\right)$. Finally, the ratio between the overall and bulk longitudinal moduli, regarded as a measure of the material stiffness reduction due to the presence of undamaged cohesive interfaces, reads as:

$$\frac{\bar{E}}{E} = \frac{1}{1+\frac{NE}{LK_n^0}} = \frac{1}{1+\frac{E}{L_{\text{mesh}}K_n^0}}. \tag{6}$$

By analyzing Eq. (6), it can be verified that the stiffness reduction can be decreased either by decreasing the cohesive interface density N/L (i.e. increasing the mesh size L_{mesh}), or increasing the initial normal cohesive stiffness K_n^0. However, both L_{mesh} and K_n^0 must be chosen such that the dimensionless quantity $\frac{E}{L_{\text{mesh}}K_n^0}$ is not excessively high, to avoid spurious traction oscillations, due to the ill-conditioning of the resulting numerical problem. Such oscillations ultimately may cause incorrect crack patterns, as already noted by de Borst et al.[42]. The resulting induced additional compliance is inversely proportional to the adopted finite element size L_{mesh}, so that the solution is found to diverge as the mesh is refined due to the varying overall elastic properties. Such an effect should be made negligible, by controlling the initial normal stiffness, i.e. by suitably calibrating its value as a function of the adopted mesh size. To this end, rather than fixing directly the value for K_n^0, it is preferable to calibrate the dimensionless normal stiffness $\kappa = K_n^0 L_{\text{mesh}}/E$, which incorporates the mesh size effects, in terms of the imposed reduction for the longitudinal modulus $R_E = \bar{E}/E < 1$. By using Eq. (6), it follows:

$$\kappa = \frac{R_E}{1-R_E}. \tag{7}$$

Once the parameter κ is computed by using Eq. (7) for a chosen R_E, the initial normal stiffness K_n^0 of the cohesive interface can be found as a function of the adopted mesh size L_{mesh}.

In a similar manner, the artificial reduction in the tangential stiffness can be investigated by considering the same plate subjected to a pure shear stress τ (see Fig. 3b). Following the above-described approach, the ratio between the overall and bulk tangential moduli can be expressed as:

$$\frac{\bar{G}}{G} = \frac{1}{1+\frac{NG}{LK_s^0}} = \frac{1}{1+\frac{G}{L_{\text{mesh}}K_s^0}} = \frac{1}{1+\frac{G}{L_{\text{mesh}}\xi K_n^0}} = \frac{1}{1+\frac{G}{E}\frac{1}{\xi\kappa}}, \tag{8}$$

having introduced a new dimensionless parameter, $\xi = K_s^0 / K_n^0$, i.e. the ratio between the tangential and normal initial stiffness coefficients of the interface. This parameter is derived from Eq. (8) after prescribing a reduction for the tangential modulus, $R_G = \bar{G}/G < 1$, which in general is different from R_E:

$$\xi = \frac{1}{2(1+\nu)\kappa} \frac{R_G}{1-R_G}, \tag{9}$$

with ν the Poisson's ratio of the bulk phase. Interestingly, it can be noted that imposing the restriction $R_E = R_G$, i.e. prescribing the same reduction for both E and G, leads to the following result:

$$\xi = \frac{G}{E} = \frac{1}{2(1+\nu)}, \tag{10}$$

implying that the ratio $\xi = K_s^0 / K_n^0$ uniquely depends on the Poisson's ratio of the bulk phase.

It is useful to highlight that Eqs. (6) and (8) may be regarded as inverse rules of mixtures for $\bar{E}$ and $\bar{G}$, respectively, thus providing lower-bounds, according to the well-known Reuss approximation applied to a laminate made of bulk and cohesive layers. It follows that Eqs. (7) and (10) can be rigorously applied for calibrating K_n^0 and K_s^0 only in the unrealistic case of aligned cohesive interfaces. To obtain "invisible" cohesive interfaces in more general situations, different semi-empirical lower bounds for κ have been proposed in the literature. For instance, Turon et al.[7] recommended values of κ larger than 50 to ensure an apparent loss of stiffness less than 2% for delamination analyses in composites. Moreover, Espinosa and Zavattieri[40] observed that, if $\kappa \geq 10$ is used, the elastic wave speeds in isotropic media is not affected by the presence of an embedded interface. A rigorous calibration criterion has been firstly introduced by Tomar et al.[41]. With reference to the 2D case, such a criterion arises from an energy equivalence condition between a discrete system made of bulk and interface elements arranged in a cross-triangle quadrilateral mesh and its equivalent homogeneous system, under three different (uniaxial, biaxial and pure shear) uniform loading conditions. Assuming plane stress conditions and $\xi = K_s^0 / K_n^0 = 1$, the following criterion for κ is obtained:

$$\kappa = \left(1+\sqrt{2}\right) \frac{R_E}{1-R_E}, \tag{11}$$

which has the same form as Eq. (7) but predicts greater values for the initial elastic stiffness at fixed R_E, due to the different spatial distribution of cohesive interfaces.

Furthermore, a more general criterion has been proposed by Blal and coworkers[43], based on an analytical micromechanical approach which uses a Hashin-Shtrikman estimate to compute the overall elastic stiffness of a medium with embedded cohesive interfaces. Such a criterion can be regarded as a generalization of the criterion (11) to the 3D case, and to any type of external loading conditions and mesh topologies. The key

principle is to consider the cohesive interfaces for a given mesh as a collection of uniformly distributed penny-shaped inclusions embedded in a continuous matrix and to obtain the overall properties of the resulting composite material as a closed-form function of bulk properties and mesh parameters (i.e. mesh topology and size). Under the assumption of isotropic overall constitutive behavior of this composite, the two dimensionless stiffness parameters κ and ξ can be computed by using the following relations:

$$\kappa = \frac{\gamma}{3(1-2\nu)}\frac{R_E}{1-R_E}, \qquad \xi = 2\frac{1-2\nu}{1+3\nu}, \tag{12}$$

obtained in [43] by enforcing the same reduction for both the moduli E and G. This restriction, implying no reduction of the Poisson's ratio, i.e. $\bar{\nu} = \nu$, guarantees the positive definiteness of the overall strain energy and is reasonable for hydrostatic loading, as discussed in [51]. The dimensionless parameter γ appearing in the first of Eqs. (12) depends on the mesh topology. Moreover, it is worth noting that the relations (12) have been also applied to planar meshes in [43]. In the case of cross-triangle quadrilateral meshes, γ has been found to be $2\left(1+\sqrt{2}\right)$ with the mesh size L_{mesh} coinciding with the side length of the square cell, whereas for an isotropic Delaunay triangulation, it has been derived the following estimate:

$$\gamma = \frac{32\sqrt{2}}{3\pi\sqrt[4]{3}} \approx 3.6485, \tag{13}$$

after having defined L_{mesh} as the edge length of an equivalent regular tessellation made of equilateral triangles (see [43] for additional details).

Unfortunately, such an approach, as most of analytical homogenization models, can only give estimates for the effective properties, and the adopted simplifying hypotheses are usually associated with unacceptable accuracy levels for real situations of practical interest. Therefore, a novel numerical homogenization scheme, described in Section 2.3, is proposed, aimed at enhancing the predictions obtained from Eq. (12).

2.3. A numerical micromechanical approach for the alleviation of mesh-induced compliance

In this section, a novel numerical micromechanical approach for the calibration of the initial (elastic) cohesive stiffness parameters is presented, able to increase the accuracy of the existing semi-empirical and analytical approaches discussed in Section 2.2. Inspired by the works of Blal and coworkers[43], we follow the idea that the bulk material with embedded cohesive interfaces may be regarded as a two-phase composite with either random or regular microstructure, depending on the topology of the finite element mesh. As a consequence, the overall elastic properties of such an assembly can be obtained by applying a sound micromechanical approach, based on the concept of representative volume element (RVE). Without loss of generality, the proposed homogenization framework will be presented in the case of planar elasticity.

In the case of a periodically structured mesh, a repeating cell (RC) is adopted as a clearly defined RVE (see Fig. 4a), whereas if an unstructured mesh is considered, the RVE is chosen as a volume containing a very large (mathematically infinite) set of bulk elements and embedded cohesive interfaces equipped with statistically homogeneous and ergodic properties (see Fig. 4b). In the former case, the RVE size L_{RVE} turns to be coincident with the mesh size L_{mesh}, whereas in the latter case, the condition $L_{\mathrm{mesh}} \ll L_{\mathrm{RVE}}$ must hold.

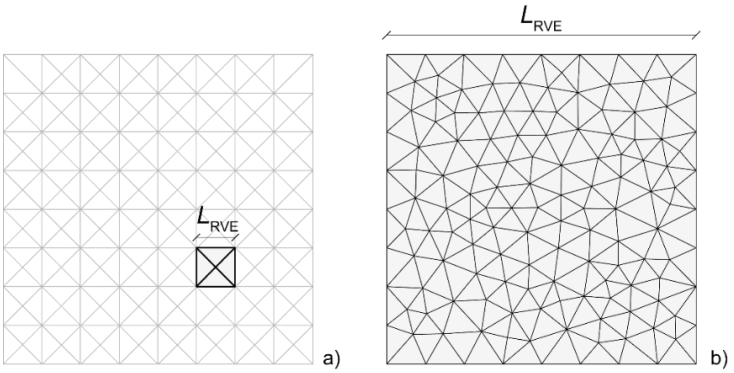

Fig. 4. Representative volume element (RVE) of a cohesive finite element assembly: (a) repeating cell (RC) for periodically structured meshes; (b) RVE for unstructured meshes.

It is well known that, if the RVE is composed of linearly elastic constituents, the following general inequalities involving the homogenized moduli tensor $\bar{\boldsymbol{C}}$ hold (see, for instance, [53] and references therein):

$$\bar{\boldsymbol{C}}^{(\mathrm{UT})}\bar{\boldsymbol{\varepsilon}} : \bar{\boldsymbol{\varepsilon}} \le \bar{\boldsymbol{C}}^{(\mathrm{G})}\bar{\boldsymbol{\varepsilon}} : \bar{\boldsymbol{\varepsilon}} \le \bar{\boldsymbol{C}}^{(\mathrm{LD})}\bar{\boldsymbol{\varepsilon}} : \bar{\boldsymbol{\varepsilon}} \tag{14}$$

for the same prescribed macro-strain $\bar{\boldsymbol{\varepsilon}}$, meaning that the homogenized moduli tensor $\bar{\boldsymbol{C}}^{(\mathrm{G})}$ obtained for general boundary conditions is always comprised between the lower and upper limit tensors, corresponding to uniform traction (UT) and linear displacement (LD) boundary conditions, respectively.

For elastic stiffness calibration purposes, we are interested in the lower bound $\bar{\boldsymbol{C}}^{(\mathrm{UT})}$, being associated with the greatest predicted value of moduli reduction among all the alternative boundary conditions. In the following, the numerically derived homogenized moduli will refer to this type of BCs.

In a two-dimensional (plane stress or strain) setting, the linearly elastic constitutive relation between the averaged stress and strain tensors, denoted by $\bar{\boldsymbol{\sigma}}$ and $\bar{\boldsymbol{\varepsilon}}$, can be expressed in the following matrix form:

$$\begin{Bmatrix} \bar{\sigma}_{11} \\ \bar{\sigma}_{22} \\ \bar{\sigma}_{12} \end{Bmatrix} = \begin{bmatrix} \bar{C}_{1111} & \bar{C}_{1122} & \bar{C}_{1112} \\ \bar{C}_{2211} & \bar{C}_{2222} & \bar{C}_{2212} \\ \bar{C}_{1211} & \bar{C}_{1222} & \bar{C}_{1212} \end{bmatrix} \begin{Bmatrix} \bar{\varepsilon}_{11} \\ \bar{\varepsilon}_{22} \\ 2\bar{\varepsilon}_{12} \end{Bmatrix}. \tag{15}$$

Owing to the assumed major symmetry of $\bar{\boldsymbol{C}}$, to solve for all the six independent components, three BVPs must be specified, by considering two uniaxial and a shear macro-strain paths in the x_1x_2 plane.

Once the homogenized moduli tensor $\bar{\boldsymbol{C}}$ is derived, representing the overall elastic properties of the discretized continuum with embedded interfaces prior to damage onset, the mesh-induced artificial compliance effect can be investigated by using a suitable compliance index, defined as follows:

$$i_c = \frac{\left\| \bar{\boldsymbol{C}} - \boldsymbol{C} \right\|}{\left\| \boldsymbol{C} \right\|}, \tag{16}$$

$\boldsymbol{C}$ being the elastic tensor of the bulk phase, and the symbol $\left\| \square \right\|$ denoting the conventional Euclidean norm of the enclosed tensor. This compliance index represents a measure of the distance between the overall moduli tensor and the elasticity tensor of the bulk phase, and therefore the condition $i_c \ll 1$ represents a necessary requirement for the cohesive/bulk aggregate to approximate the original continuum.

It is worth noting that the homogenized moduli tensor $\bar{\boldsymbol{C}}$ is anisotropic in general, and the anisotropy level is expected to be dependent on the mesh topology as well as on the adopted values for the initial cohesive stiffness parameters K_n^0 and K_s^0 (or their dimensionless counterparts κ and ξ). In order to measure the anisotropy induced by the presence of embedded interfaces, the following anisotropy index is introduced:

$$i_a = \frac{\left\| \bar{\boldsymbol{C}} - \bar{\boldsymbol{C}}^{\mathrm{iso}} \right\|}{\left\| \bar{\boldsymbol{C}}^{\mathrm{iso}} \right\|}, \tag{17}$$

where $\bar{\boldsymbol{C}}^{\mathrm{iso}}$ is the isotropic moduli tensor closest to $\bar{\boldsymbol{C}}$. A second requirement for the invisibility of embedded interfaces is that the condition $i_a \ll 1$ remains valid, after choosing K_n^0 and K_s^0. Requirements for both indexes (16) and (17) will be verified a posteriori in the simulations, as shown in Section 4.2.

The problem of determining $\bar{\boldsymbol{C}}^{\mathrm{iso}}$ can be regarded as a particular version of the more general problem of finding the closest approximation of an elasticity tensor with arbitrary material symmetry to an elasticity tensor with given symmetry, which has been largely investigated. Several metrics have been proposed in the literature to determine the distance between two arbitrary elasticity tensors (see, for instance, [54]). The most widely used metric is the Euclidean metric, denoted by $d_E\left(\boldsymbol{C}_1, \boldsymbol{C}_2\right) = \left\| \boldsymbol{C}_1 - \boldsymbol{C}_2 \right\|$. Accordingly, a good candidate for such an equivalent isotropic elasticity tensor is the projection of the homogenized moduli tensor $\bar{\boldsymbol{C}}$ onto the class C^{iso} of isotropic elasticity tensors, computed by using the distance d_E, such that:

$$\bar{\boldsymbol{C}}^{iso} = \underset{\bar{\boldsymbol{C}}^* \in C^{\mathrm{iso}}}{\mathrm{Arg\,min}}\, d_E\left(\bar{\boldsymbol{C}}, \bar{\boldsymbol{C}}^*\right). \tag{18}$$

Equivalently, the closest isotropic homogenized 2D moduli, i.e. the planar bulk modulus $\bar{K}_{2\mathrm{D}}$ and shear modulus $\bar{G}_{2\mathrm{D}}$ can be obtained by the following double minimization problem:

$$\left(\bar{K}_{2D},\bar{\mu}_{2D}\right)=\underset{\bar{K}^{*}_{2D},\bar{\mu}^{*}_{2D}}{\mathrm{Arg}\min}\, d_E\left(\bar{\boldsymbol{C}},\bar{\boldsymbol{C}}^{*}\left(\bar{K}^{*}_{2D},\bar{\mu}^{*}_{2D}\right)\right) \tag{19}$$

with respect to the unknowns $\bar{K}^{*}_{2D}$ and $\bar{G}^{*}_{2D}$, leading to the following expressions:

$$\begin{aligned}\bar{K}_{2D}&=\frac{1}{2}\left(\bar{C}^{\mathrm{iso}}_{1111}+\bar{C}^{\mathrm{iso}}_{1122}\right)=\frac{1}{4}\left(\bar{C}_{1111}+\bar{C}_{2222}+2\bar{C}_{1122}\right)\\ \bar{G}_{2D}&=\frac{1}{2}\left(\bar{C}^{\mathrm{iso}}_{1111}-\bar{C}^{\mathrm{iso}}_{1122}\right)=\frac{1}{8}\left(\bar{C}_{1111}+\bar{C}_{2222}-2\bar{C}_{1122}+4\bar{C}_{1212}\right)\end{aligned}, \tag{20}$$

which can be regarded as the 2D counterpart of the relations for 3D elasticity reported in [54]. It is worth noting that these isotropized moduli do not depend on the moduli $\bar{C}_{1112}$ and $\bar{C}_{2212}$.

Then, the planar bulk modulus $\bar{K}_{2D}$ can be expressed as a function of the homogenized Young's modulus $\bar{E}$ and Poisson's ratio $\bar{\nu}$, as follows:

$$\bar{K}_{2D}=\frac{\bar{E}'}{2(1-\bar{\nu}')}\qquad \bar{E}'=\begin{cases}\bar{E} & \text{plane stress}\\ \dfrac{\bar{E}}{1-\bar{\nu}^{2}} & \text{plane strain}\end{cases}\qquad \bar{\nu}'=\begin{cases}\bar{\nu} & \text{plane stress}\\ \dfrac{\bar{\nu}}{1-\bar{\nu}} & \text{plane strain}\end{cases}. \tag{21}$$

According to Eq. (21) one must specify either plane-strain or plane-stress states to express the planar bulk modulus, whilst $\bar{G}_{2D}$ is equal to the usual shear modulus $\bar{G}$, either in plane-strain or plane-stress elasticity:

$$\bar{G}_{2D}=\bar{G}=\frac{\bar{E}}{2(1+\bar{\nu})}. \tag{22}$$

The isotropized overall moduli tensor $\bar{C}^{\mathrm{iso}}_{ijkl}$ can be alternatively derived by using an angular averaging technique, which leads to perfectly equivalent results as the minimization problem (18). With reference to planar elasticity, the homogenized (anisotropic) moduli tensor $\bar{C}_{ijkl}$ can be analytically averaged over the single polar angle ϕ, using a proper orthogonal transformation Q_{ij} with the following matrix representation:

$$\left[\boldsymbol{Q}\right]=\begin{bmatrix}\cos\phi & \sin\phi\\ -\sin\phi & \cos\phi\end{bmatrix}. \tag{23}$$

In the 2D setting, the angularly averaged overall moduli tensor $\left\langle\bar{\boldsymbol{C}}\right\rangle_{\phi}$ is then:

$$\left\langle\bar{C}_{ijkl}\right\rangle_{\phi}=\frac{1}{2\pi}\sum_{mnpq}\bar{C}_{mnpq}\int_{0}^{2\pi}Q_{mi}Q_{nj}Q_{pk}Q_{ql}\,d\phi\qquad (m,n,p,q=1,2). \tag{24}$$

It can be easily shown that $\left\langle \bar{\boldsymbol{C}} \right\rangle_{\phi}$ turns to be isotropic and coincides with the closest isotropic homogenized moduli tensor $\bar{\boldsymbol{C}}^{\text{iso}}$, whose matrix representation (in Voigt notation) is:

$$\left[\bar{\boldsymbol{C}}^{\text{iso}}\right] = \begin{bmatrix} \bar{C}^{\text{iso}}_{1111} & \bar{C}^{\text{iso}}_{1122} & 0 \\ \bar{C}^{\text{iso}}_{1122} & \bar{C}^{\text{iso}}_{1111} & 0 \\ 0 & 0 & \frac{1}{2}\left(\bar{C}^{\text{iso}}_{1111} - \bar{C}^{\text{iso}}_{1122}\right) \end{bmatrix}. \tag{25}$$

Assuming that the anisotropy index (17) is much smaller than one, meaning that homogenized medium remains almost isotropic, the artificial compliance associated with the embedded cohesive interfaces can be measured by considering $\bar{\boldsymbol{C}}^{\text{iso}}$ rather than $\bar{\boldsymbol{C}}$. Therefore, instead of the compliance index (16), the moduli reductions $R_E = \bar{E}/E$ and $R_\nu = \bar{\nu}/\nu$ have been used in the present work to calibrate the stiffness parameters of the embedded cohesive interfaces. Once these reductions are fixed, the resulting system of nonlinear equations to be solved in the two unknown κ and ξ takes the following form:

$$\begin{cases} R_E = R_E\left(\kappa, \xi\right) \\ R_\nu = R_\nu\left(\kappa, \xi\right) \end{cases}. \tag{26}$$

Some general results concerning the calibration of the cohesive stiffness parameters in the case of random mesh configurations will be reported in Section 4.1.

3. DESCRIPTION OF THE DIFFUSE INTERFACE MODEL

Multiple crack initiation and propagation in concrete-like structures is accounted for via a diffuse interface model (DIM), based on the cohesive finite element method presented in Section 2.1. The main advantage of this approach is that no mesh updates are required, unlike for many classical discrete crack approaches. A fundamental preprocessing operation for the adopted inter-element fracture approach is the construction of the cohesive/volumetric finite element mesh. This operation, performed automatically by exploiting the advanced scripting capabilities of the adopted numerical environment[55], will be detailed in the companion Part II paper[56]. The mechanical behavior of the embedded interfaces is governed by an isotropic damage cohesive law $\boldsymbol{t}_{\text{coh}} = \left(1-d\right)\boldsymbol{K}_0 \ \boldsymbol{u}$, written in the matrix form as follows:

$$\begin{Bmatrix} t_n^{\text{coh}} \\ t_s^{\text{coh}} \end{Bmatrix} = \left(1-d\right)\begin{bmatrix} K_n^0 & 0 \\ 0 & K_s^0 \end{bmatrix}\begin{Bmatrix} \delta_n \\ \delta_s \end{Bmatrix}, \tag{27}$$

the subscripts n and s referring to the normal and tangential directions, respectively. It is worth noting that the off-diagonal stiffness terms are zero in the assumed constitutive law, meaning that the dilatancy effects are totally neglected. The scalar damage variable d appearing in Eq. (27) possesses the following

linear-exponential evolution law, already used in [44], involving the (mixed-mode) effective displacement jump $\delta_m = \sqrt{\langle \delta_n \rangle^2 + \delta_s^2}$ (with the symbol $\langle \square \rangle$ denoting the positive part of the enclosed quantity):

$$d = \begin{cases} 0 & \text{for } \delta_m^{\max} \le \delta_m^0 \\ 1 - \dfrac{\delta_m^0}{\delta_m^{\max}} \left\{ 1 - \dfrac{1 - \exp\left[-\alpha \left(\dfrac{\delta_m^{\max} - \delta_m^0}{\delta_m^f - \delta_m^0} \right) \right]}{1 - \exp(-\alpha)} \right\} & \text{for } \delta_m^0 < \delta_m^{\max} \le \delta_m^f \\ 1 & \text{for } \delta_m^{\max} > \delta_m^f \end{cases}, \tag{28}$$

where δ_m^0 and δ_m^f are the effective displacement jumps at damage onset and total decohesion, respectively, $\delta_m^{\max}$ denotes the maximum value attained by the effective displacement jump over the entire loading history, and α is a dimensionless material parameter influencing the rate of damage evolution with $\delta_m^{\max}$.

The mixed-mode crack initiation is governed by a stress-based quadratic interaction criterion (valid only for $\delta_n > 0$), leading to the following definition for δ_m^0:

$$\delta_m^0 = \delta_n^0 \delta_s^0 \sqrt{\frac{1+\beta^2}{\left(\delta_s^0\right)^2 + \left(\beta \delta_n^0\right)^2}}, \tag{29}$$

where $\delta_n^0 = \sigma_{\max} / K_n^0$ and $\delta_s^0 = \tau_{\max} / K_s^0$, $\sigma_{\max}$ and $\tau_{\max}$ denoting the normal and tangential critical interface stresses, whereas $\beta = \delta_s / \delta_n$ is the ratio between the tangential and normal displacement jumps.

The mixed-mode crack propagation is governed by the following linear power law criterion (also valid only for $\delta_n > 0$), involving the two in-plane modal components G_{I} and G_{II} of the energy release rate:

$$\frac{G_{\mathrm{I}}}{G_{\mathrm{Ic}}} + \frac{G_{\mathrm{II}}}{G_{\mathrm{IIc}}} = 1, \tag{30}$$

G_{Ic} and G_{IIc} being the mode-I and mode-II fracture energies, respectively. The energy release rates corresponding to total decohesion in mixed mode are (see [6] for additional details about their derivation):

$$\begin{aligned} G_{\mathrm{I}} &= \frac{K_n^0}{2\left(1+\beta^2\right)} \left(\left(\delta_m^0\right)^2 + \frac{2\left(1+\alpha-e^{\alpha}\right)}{\alpha\left(1-e^{\alpha}\right)} \delta_m^0 \left(\delta_m^f - \delta_m^0\right) \right) \\ G_{\mathrm{II}} &= \frac{\beta^2 K_s^0}{2\left(1+\beta^2\right)} \left(\left(\delta_m^0\right)^2 + \frac{2\left(1+\alpha-e^{\alpha}\right)}{\alpha\left(1-e^{\alpha}\right)} \delta_m^0 \left(\delta_m^f - \delta_m^0\right) \right) \end{aligned}. \tag{31}$$

By inserting Eq. (31) into Eq. (30), and solving the equation with respect to δ_m^f, the mixed-mode displacement jump corresponding to total decohesion is obtained as:

$$\delta_m^f = \frac{\alpha\left(1-e^{\alpha}\right)}{2\left(1+\alpha-e^{\alpha}\right)}\left[\frac{2\left(1+\beta^2\right)}{\delta_m^0}\left(\frac{K_n^0}{G_{\mathrm{Ic}}}+\frac{\beta^2 K_s^0}{G_{\mathrm{IIc}}}\right)^{-1}-\left(1-\frac{2\left(1+\alpha-e^{\alpha}\right)}{\alpha\left(1-e^{\alpha}\right)}\right)\delta_m^0\right]. \tag{32}$$

When $\delta_n \le 0$, a pure mode-II fracture occurs (i.e. $G_{\mathrm{I}} = 0$), and the related crack advancement criterion reads as $G_{\mathrm{II}} = G_{\mathrm{IIc}}$. The mode-II energy release rate corresponding to total decohesion is:

$$G_{\mathrm{II}} = \frac{K_s^0}{2}\left(\left(\delta_s^0\right)^2+\frac{2\left(1+\alpha-e^{\alpha}\right)}{\alpha\left(1-e^{\alpha}\right)}\delta_s^0\left(\delta_s^f-\delta_s^0\right)\right). \tag{33}$$

By equating the expression (33) to G_{IIc}, and solving with respect to δ_s^f, the mode-II displacement jump corresponding to total decohesion is found as:

$$\delta_s^f = \frac{\alpha\left(1-e^{\alpha}\right)}{2\left(1+\alpha-e^{\alpha}\right)}\left[\frac{2G_{\mathrm{IIc}}}{K_s^0\delta_s^0}-\left(1-\frac{2\left(1+\alpha-e^{\alpha}\right)}{\alpha\left(1-e^{\alpha}\right)}\right)\delta_s^0\right]. \tag{34}$$

It is worth noting that the adopted cohesive law cannot predict damage under pure compression, and does not incorporate any friction model. Moreover, interpenetration is prevented by adding a unilateral contact constraint enforced via a penalty method, which adopts the value K_n^0 as regularization parameter.

4. NUMERICAL VALIDATION OF THE DIFFUSE INTERFACE MODEL

In this section, the adopted diffuse interface model is validated in both linear and nonlinear regimes. In particular, in Section 4.1, the elastic stiffness parameters for obtaining invisible cohesive interfaces are obtained using the micromechanical approach described in Section 2.3. In Section 4.2, a further analysis of both compliance and anisotropy levels for the resulting overall homogenized moduli is given. Finally, in Section 4.3, the mesh-induced toughening effect during crack propagation is investigated by comparing the present model with other mesh-independent fracture approaches, explicitly introduced as the reference.

4.1. Calibration of the initial cohesive stiffness parameters

Here, some general results are reported concerning the elastic calibration of diffuse interface model (DIM), described in Section 3, with reference to planar unstructured meshes, plane stress and uniform traction boundary conditions. The numerical homogenization technique presented in Section 2.3 is adopted to obtain the present results. It is worth recalling that this type of boundary conditions is chosen, since it provides the smallest overall moduli among those that satisfy the Hill-Mandel's condition, associated with the greatest

estimated artificial compliance. It follows that, under general boundary conditions, the resulting loss of stiffness induced by the embedded interfaces is assured to be always smaller than the prescribed one.

In detail, a circular RVE with diameter $D = L_{\mathrm{RVE}}$ is considered, consisting in a Delaunay triangulation with n_e three-node finite elements and embedded four-node interface elements (the insertion procedure will be detailed in the companion Part 2 paper[56]). This RVE can be intended as the sample of a polycrystalline material with randomly distributed triangular grains and elastic grain boundaries. Although this RVE has not the space-filling property of usual tetragonal and hexagonal RVEs, it is chosen to avoid preferential directions for the mesh generation, by virtue of the absence of corners. The characteristic (average) mesh size L_{mesh}, coinciding with the edge length of an equivalent equilateral triangulation, can be expressed as:

$$L_{\mathrm{mesh}} = \sqrt{\frac{\pi D^2}{n_e \sqrt{3}}} \,. \tag{35}$$

and should be much smaller than L_{RVE} for the homogenized moduli to be correctly computed. In order to determine the mesh size L_{mesh} to be used for homogenization purposes, different mesh resolutions are considered, with number n_e of finite elements varying from 110 to 8364. These preliminary numerical computations are addressed to a concrete-like material with bulk elastic constants $E = 30$ GPa and $\nu = 0.2$, whose cohesive interfaces are calibrated by preliminarily assigning $\xi = 1$. Fig. 5a shows the results of the mesh sensitivity analysis in terms of convergence of the overall Young's modulus $\bar{E}$, for different values of κ belonging to a wide range, as a function of the dimensionless parameter $\rho = L_{\mathrm{RVE}} / L_{\mathrm{mesh}}$, which is a proper measure of the distance between the RVE scale and the finite element scale. The mesh associated with $\rho = 36.5$, shown in Fig. 5b, is chosen for obtaining the following numerical homogenization results, being the coarsest mesh assuring a percentage variation of the overall Young's modulus $\bar{E}$, defined as:

$$e_E = \frac{\bar{E} - \bar{E}_{\mathrm{ref}}}{\bar{E}_{\mathrm{ref}}} \times 100 \,, \tag{36}$$

smaller than 1% compared to the finest mesh resolution (corresponding to the reference value $\rho_{\mathrm{ref}} = 67.9$), for any considered value of κ. It is also verified that this mesh density is sufficient to achieve a numerical accuracy of about 1% on the statistical fluctuations associated with many RVE realizations. These results, obtained by statistical analyses similar to those performed in [57], are not reported for the sake of brevity.

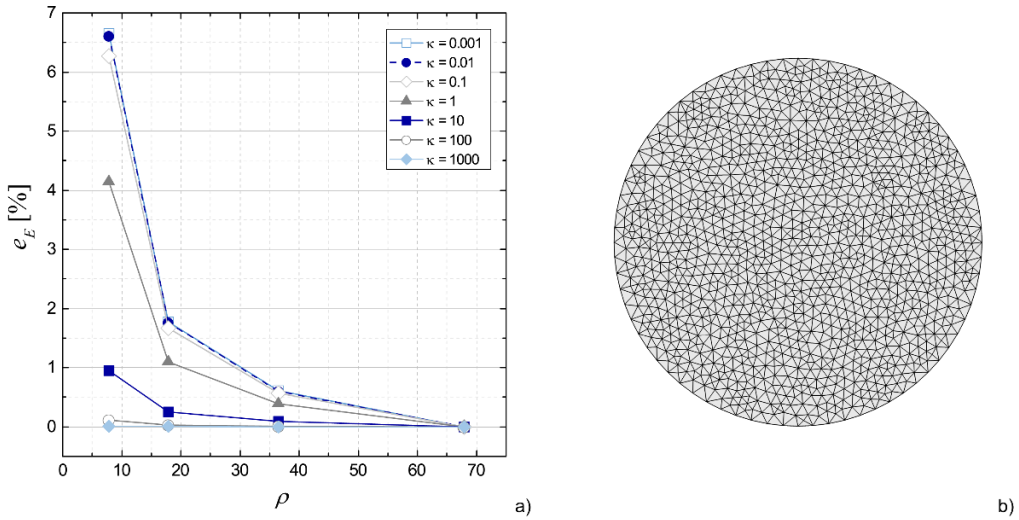

Fig. 5. Mesh convergence analysis for homogenization purposes: (a) percentage variation of the overall Young's modulus vs dimensionless RVE size; (b) adopted mesh configuration for the calibration of the cohesive interface model (having $\rho = L_{\mathrm{RVE}} / L_{\mathrm{mesh}} = 36.5$).

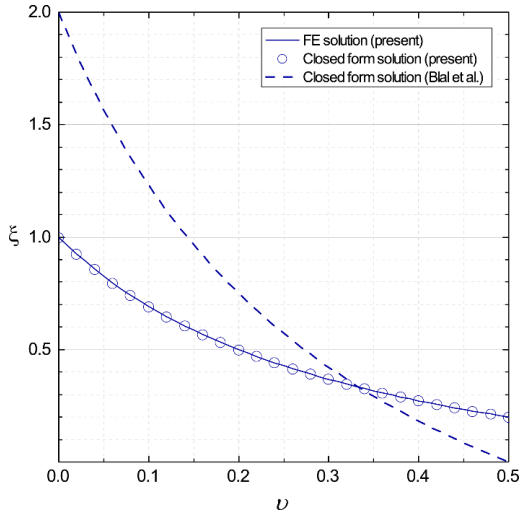

Fig. 6. Tangential-to-normal stiffness ratio as a function of the Poisson's ratio: comparisons between the present results, in terms of both numerical and closed-form according to Eq. (37), and those found in [43].

Once the RVE size is found, the calibration of the elastic stiffness parameters of the embedded interfaces is performed by solving the system (26) for the couple (κ, ξ) in an iterative manner, after prescribing suitable values to R_E and R_ν. It is found that the choice $R_\nu = 1$ (no reduction of the Poisson's ratio) allows the dependence of R_ν on κ to be practically neglected, coherently with what has been predicted by Eq. (10). It follows that the ratio ξ between the tangential and normal stiffness parameters can be regarded as a function of only the Poisson's ratio of the bulk phase, whose numerically derived behavior is shown in Fig. 6. Moreover, the following closed-form solution has been found, also depicted in Fig. 6, having the best fit of the numerically derived points:

$$\xi = \frac{1-\nu}{1+3\nu}, \tag{37}$$

which can be regarded as the 2D counterpart (under plane stress conditions) of the latter of Eqs. (12), which was derived in [43] for the 3D case (although also applied to planar elasticity problems). It is interesting to note that, in contrast to what is predicted by the latter of Eqs. (12), also reported in Fig. 6 for comparison purposes, the tangential-to-normal stiffness ratio to be assigned according the proposed calibration method is always smaller than one (this limit value is reached for $\nu = 0$). Moreover, for incompressible materials (i.e. $\nu = 0.5$), the present result predicts no vanishing behavior for ξ.

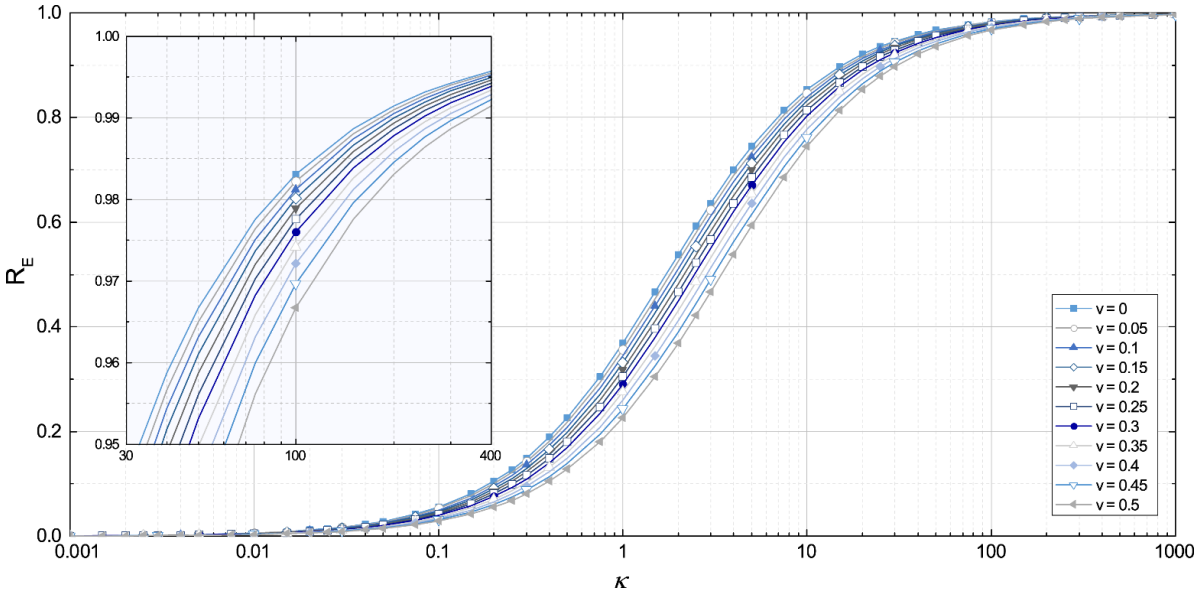

Fig. 7. Dimensionless normal stiffness vs Young's modulus reduction chart.

By introducing Eq. (37) in the first of Eqs. (26), it follows that κ can be found as a function of the desired reduction R_E and of the given Poisson's ratio. Several numerical computations have been performed to create the chart shown in Fig. 7, which is valid for any isotropic and linear elastic material with $0 \le \nu < 0.5$ subjected to a plane stress state. This chart numerically confirms the qualitative behavior of the first of Eqs. (12), being characterized by $\lim_{\kappa \to 0} R_E = 0$ and $\lim_{\kappa \to \infty} R_E = 1$, but provides more reliable results for greater Poisson's ratios. As a matter of fact, the first of Eqs. (12) loses its meaning for perfectly incompressible materials, predicting an infinite cohesive stiffness for any reduction of the Young's modulus.

The most useful part of this chart is the top one, extracted and reported in the same Fig. 7, referring to values of R_E greater than 0.95 (assuming a stiffness reduction of 5% admissible for engineering purposes). The value of κ assuring a prescribed threshold value of R_E is the abscissa of the intersection point between the horizontal line passing through this threshold and the curve associated with the given Poisson's ratio.

4.2. Evaluation of the mesh-induced compliance and anisotropy levels

To assess the general validity of the proposed calibration methodology, a numerical investigation of both compliance and anisotropy levels induced by the mesh is performed, by computing the two indices (16) and (17), introduced in Section 2.3, for different values of both κ and ν within the considered ranges.

As shown in Table 1, the variation of the Poisson's ratio has a limited influence on the compliance index i_c, which tends to slightly increase for increasing values of ν at fixed κ. Contrarily, as expected, i_c is strongly affected by the elastic stiffness of the cohesive interface, providing unacceptable compliance increments (greater than 5%) for values of κ smaller than 20, regardless of the adopted Poisson's ratio.

The variation of the anisotropy index i_a within the same ranges of independent variables is reported in Table 2. As expected, for any value of ν, a decrease of the stiffness parameter κ leads to an increase of the mesh-induced anisotropy level, which, however, does not exceed 1%. This value confirms the effectiveness of the proposed micromechanical calibration with respect to the desired isotropy requirement.

It is useful to highlight that the preliminary numerical results reported in Figs. 6 and 7 and in Tables 1 and 2 are valid for any isotropic material with Poisson's ratio ranging from 0 to 0.5. In the particular case $\nu = 0.2$, which is typical for concrete, further numerical results are presented, aimed at better investigating the mesh-induced effects on the homogenized moduli.

Fig. 8 shows the behavior of the (plane stress) homogenized moduli for the given cohesive finite element assembly as a function of the normal stiffness parameter of the embedded interfaces. All the moduli are normalized with respect to the Young's modulus of the bulk. It can be noted that for any value of κ, the cohesive finite element assembly preserves its isotropy, thus assuring the same loss of stiffness in each direction. This effect is essentially due to the adopted (isotropic) mesh topology, for which the embedded cohesive interfaces are randomly placed without introducing any preferential orientation into the model.

Table 1. Compliance index as a function of both the bulk Poisson's ratio and the dimensionless normal stiffness of the cohesive interface.

		ν										
		0	0.05	0.1	0.15	0.2	0.25	0.3	0.35	0.4	0.45	0.5
κ	0.001	0.9994	0.9994	0.9995	0.9995	0.9995	0.9996	0.9996	0.9996	0.9996	0.9997	0.9997
	0.002	0.9988	0.9989	0.9989	0.9990	0.9991	0.9991	0.9992	0.9992	0.9993	0.9994	0.9994
	0.005	0.9971	0.9972	0.9974	0.9975	0.9977	0.9978	0.9980	0.9981	0.9983	0.9984	0.9985
	0.01	0.9942	0.9945	0.9948	0.9951	0.9953	0.9956	0.9959	0.9962	0.9965	0.9968	0.9971
	0.02	0.9884	0.9890	0.9896	0.9902	0.9907	0.9913	0.9919	0.9925	0.9930	0.9936	0.9942
	0.05	0.9716	0.9730	0.9744	0.9758	0.9772	0.9786	0.9800	0.9814	0.9828	0.9842	0.9856
	0.1	0.9448	0.9474	0.9500	0.9527	0.9553	0.9580	0.9607	0.9634	0.9661	0.9689	0.9716
	0.2	0.8954	0.9001	0.9048	0.9096	0.9145	0.9194	0.9244	0.9294	0.9345	0.9397	0.9449
	0.5	0.7741	0.7829	0.7919	0.8012	0.8107	0.8204	0.8303	0.8405	0.8510	0.8617	0.8727
	1	0.6316	0.6434	0.6557	0.6685	0.6818	0.6956	0.7100	0.7250	0.7407	0.7571	0.7743
	2	0.4618	0.4745	0.4880	0.5023	0.5174	0.5335	0.5506	0.5689	0.5884	0.6094	0.6318
	5	0.2557	0.2656	0.2762	0.2878	0.3004	0.3141	0.3292	0.3457	0.3641	0.3845	0.4073
	10	0.1467	0.1532	0.1603	0.1682	0.1768	0.1864	0.1971	0.2091	0.2227	0.2381	0.2559
	20	0.0792	0.0830	0.0872	0.0919	0.0970	0.1028	0.1094	0.1168	0.1253	0.1352	0.1468
	50	0.0333	0.0349	0.0368	0.0389	0.0412	0.0439	0.0468	0.0503	0.0542	0.0589	0.0644
	100	0.0169	0.0178	0.0188	0.0198	0.0211	0.0224	0.0240	0.0258	0.0279	0.0303	0.0333
	200	0.0085	0.0090	0.0095	0.0100	0.0106	0.0113	0.0121	0.0131	0.0141	0.0154	0.0169
	500	0.0034	0.0036	0.0038	0.0040	0.0043	0.0046	0.0049	0.0053	0.0057	0.0062	0.0068
	1000	0.0017	0.0018	0.0019	0.0020	0.0021	0.0023	0.0025	0.0026	0.0029	0.0031	0.0034

Table 2. Anisotropy index as a function of both the bulk Poisson's ratio and the dimensionless normal stiffness of the cohesive interface.

		ν										
		0	0.05	0.1	0.15	0.2	0.25	0.3	0.35	0.4	0.45	0.5
κ	0.001	4.548E-3	4.389E-3	4.217E-3	4.031E-3	3.832E-3	3.620E-3	3.396E-3	3.161E-3	2.918E-3	2.669E-3	2.414E-3
	0.002	4.545E-3	4.386E-3	4.214E-3	4.029E-3	3.830E-3	3.618E-3	3.394E-3	3.160E-3	2.917E-3	2.668E-3	2.413E-3
	0.005	4.537E-3	4.379E-3	4.207E-3	4.023E-3	3.824E-3	3.613E-3	3.390E-3	3.157E-3	2.914E-3	2.665E-3	2.411E-3
	0.01	4.523E-3	4.366E-3	4.196E-3	4.012E-3	3.815E-3	3.605E-3	3.383E-3	3.150E-3	2.909E-3	2.661E-3	2.408E-3
	0.02	4.496E-3	4.342E-3	4.174E-3	3.992E-3	3.797E-3	3.589E-3	3.369E-3	3.138E-3	2.898E-3	2.652E-3	2.400E-3
	0.05	4.417E-3	4.269E-3	4.107E-3	3.932E-3	3.743E-3	3.541E-3	3.327E-3	3.102E-3	2.867E-3	2.626E-3	2.379E-3
	0.1	4.292E-3	4.153E-3	4.002E-3	3.836E-3	3.657E-3	3.464E-3	3.259E-3	3.043E-3	2.817E-3	2.583E-3	2.343E-3
	0.2	4.061E-3	3.940E-3	3.806E-3	3.658E-3	3.496E-3	3.320E-3	3.132E-3	2.932E-3	2.721E-3	2.502E-3	2.276E-3
	0.5	3.497E-3	3.414E-3	3.319E-3	3.210E-3	3.088E-3	2.953E-3	2.804E-3	2.642E-3	2.470E-3	2.287E-3	2.095E-3
	1	2.840E-3	2.793E-3	2.735E-3	2.666E-3	2.585E-3	2.492E-3	2.387E-3	2.269E-3	2.140E-3	2.000E-3	1.850E-3
	2	2.064E-3	2.047E-3	2.024E-3	1.991E-3	1.950E-3	1.900E-3	1.839E-3	1.769E-3	1.689E-3	1.599E-3	1.500E-3
	5	1.134E-3	1.137E-3	1.136E-3	1.132E-3	1.123E-3	1.109E-3	1.090E-3	1.065E-3	1.035E-3	9.986E-4	9.564E-4
	10	6.472E-4	6.525E-4	6.562E-4	6.579E-4	6.573E-4	6.543E-4	6.486E-4	6.401E-4	6.287E-4	6.141E-4	5.963E-4
	20	3.482E-4	3.523E-4	3.557E-4	3.580E-4	3.594E-4	3.595E-4	3.585E-4	3.560E-4	3.522E-4	3.469E-4	3.401E-4
	50	1.459E-4	1.480E-4	1.498E-4	1.512E-4	1.523E-4	1.529E-4	1.530E-4	1.527E-4	1.518E-4	1.505E-4	1.486E-4
	100	7.416E-5	7.527E-5	7.624E-5	7.705E-5	7.767E-5	7.809E-5	7.827E-5	7.823E-5	7.794E-5	7.742E-5	7.666E-5
	200	3.738E-5	3.796E-5	3.847E-5	3.890E-5	3.923E-5	3.947E-5	3.959E-5	3.960E-5	3.950E-5	3.928E-5	3.895E-5
	500	1.503E-5	1.526E-5	1.547E-5	1.565E-5	1.579E-5	1.589E-5	1.595E-5	1.596E-5	1.593E-5	1.585E-5	1.573E-5
	1000	7.525E-6	7.644E-6	7.750E-6	7.839E-6	7.911E-6	7.962E-6	7.992E-6	8.000E-6	7.986E-6	7.949E-6	7.891E-6

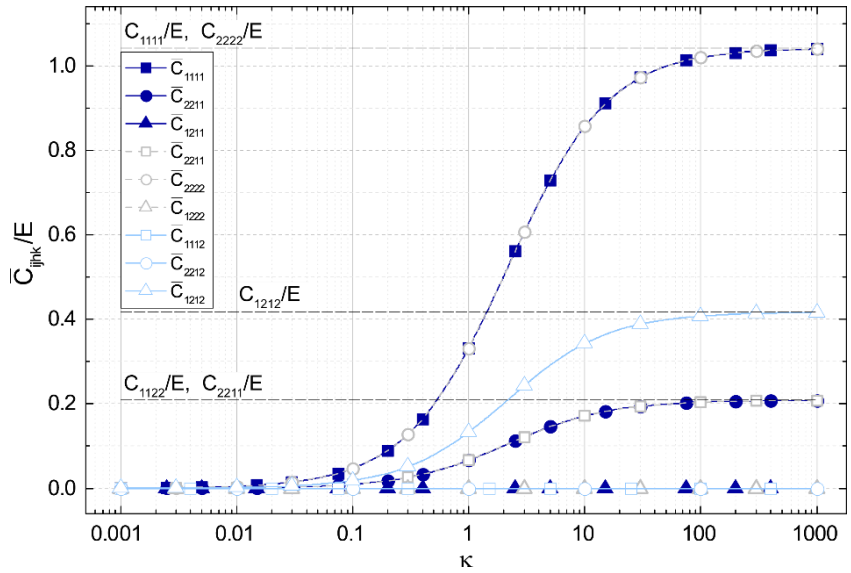

Fig. 8. Homogenized moduli for a cohesive finite element assembly (plane stress assumption and $\nu = 0.2$) as a function of the normal stiffness parameter of the embedded interfaces (dashed lines refer to the corresponding bulk moduli).

A deeper investigation of the mesh-induced anisotropy associated with the DIM approach is provided by computing the effective moduli for several mesh orientations in the x_1x_2 plane. The rotated moduli $\bar{\boldsymbol{C}}^*$ are computed applying the transformation (23) to the moduli $\bar{\boldsymbol{C}}$ referring to the x_1x_2 directions:

For each considered orientation and for different values of the normal stiffness parameter, the percentage deviation of the overall moduli with respect to their angularly averaged counterpart has been computed as:

$$e_C = \frac{\bar{C}^*_{ijkl} - \left\langle \bar{C}_{ijkl} \right\rangle_\phi}{\left\langle \bar{C}_{ijkl} \right\rangle_\phi} \times 100\,, \tag{38}$$

$\left\langle \bar{C}_{ijkl} \right\rangle_{\phi}$ being obtained by means of Eq. (24). The numerical computed deviations for the principal moduli, reported in Fig. 9, are always very small (in the worst case less than 0.5%), thus further confirming the effectiveness of the proposed calibration methodology with respect to the desired isotropy property. As expected, this deviation tends to decrease for increasing values of the stiffness parameter. Interestingly, it can be noted also that the deviation for the macroscopic moduli $\bar{C}_{1122} = \bar{C}_{2211}$ and $\bar{C}_{1212}$ are always negligible for any value of κ, meaning that, even in the presence of soft embedded elastic interfaces, the shear constitutive response preserves its perfect isotropy. It is worth noting that the present numerical outcomes refer to the (isotropic) Delaunay mesh depicted in Fig. 5b. The adoption of different meshes, without isotropic properties, would probably introduce a more evident dependency of the homogenized moduli on the mesh orientation, but this investigation is outside of the scopes of the present work.

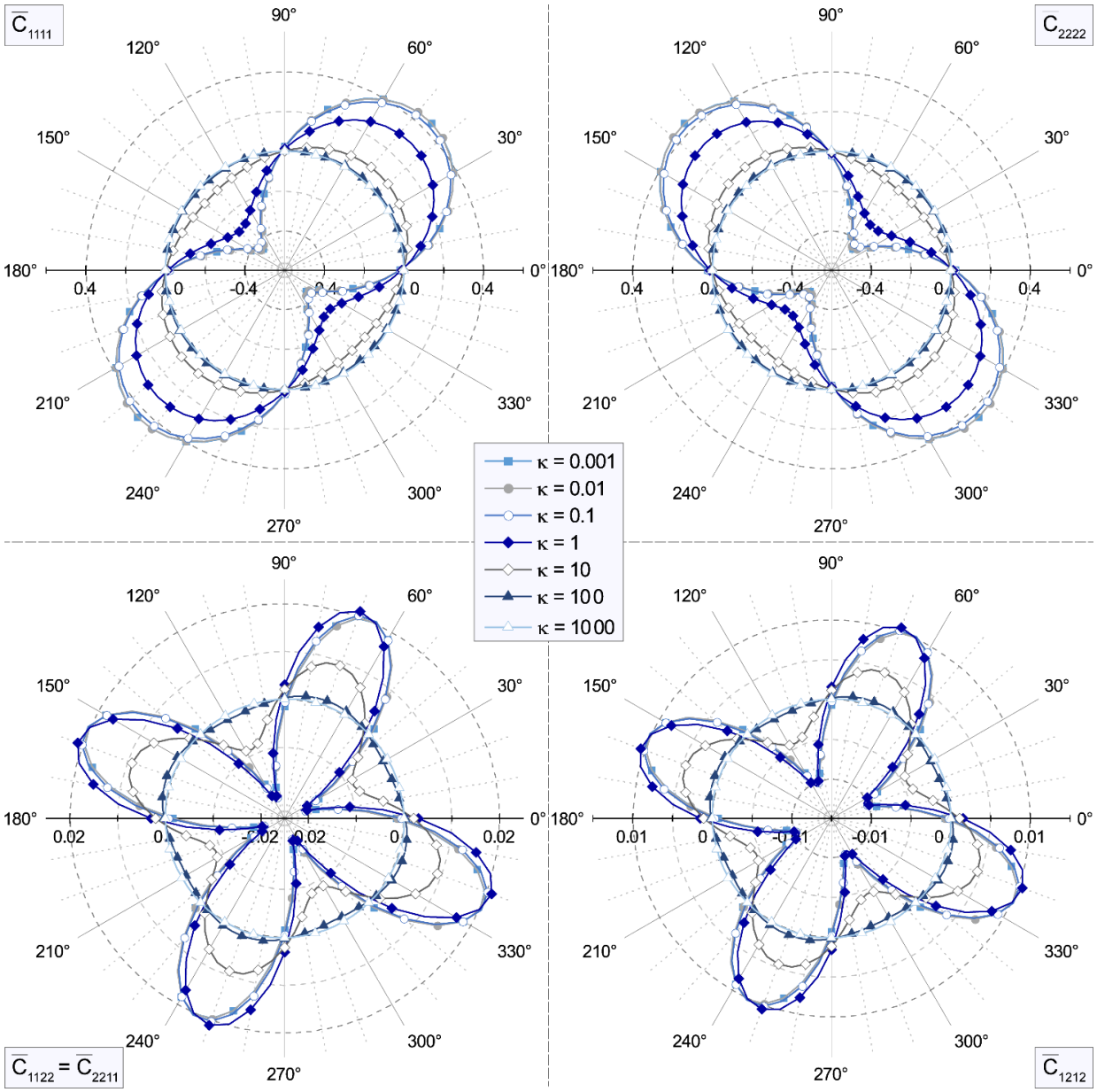

Fig. 9. Percentage deviation of the homogenized moduli with respect to their angularly averaged counterpart vs mesh orientation for different values of the normal stiffness parameter κ.

4.3. Investigation of the mesh-induced toughening effect

The numerical simulations reported here are conducted to validate the adopted diffuse interface model in the nonlinear range, with reference to concrete-like structures subjected to mode-I loading conditions. To this end, the simply supported notched beam subjected to a three-point bending test, already analyzed in [58], is considered. The geometric configuration and the boundary conditions of the simulated beam are depicted in Fig. 10, the beam height H being set equal to 0.2 m. Moreover, in order to reduce the computational cost of the numerical simulations, the cohesive elements are inserted only in a circular region with radius $r = 0.24H$ placed ahead the notch. A suitable mesh refinement has been performed inside this region, using a uniform (isotropic) Delaunay tessellation and imposing a maximum edge length of 4 mm, which results in an average mesh size of about 2.63 mm.

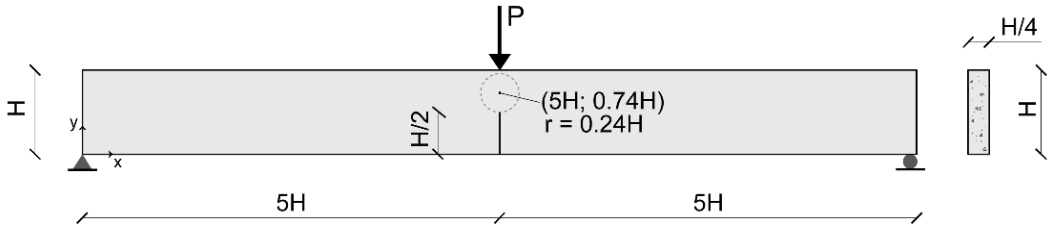

Fig. 10. Geometry and boundary conditions for the three-point bending test.

The Young's modulus and the Poisson's ratio of the bulk are equal to 30 GPa and 0.18, respectively, whilst the cohesive properties of the embedded interfaces, required by the mixed-mode constitutive law described in Section 3, are reported in Table 3. In particular, α has been set equal to 5, which is a suitable value for concrete. More sophisticated calibration methodologies for the inelastic cohesive parameters have been proposed in the literature, such as the data reduction procedure proposed in [59] or the probabilistic parameter calibration adopted in [60], but an accurate inverse identification of these parameters starting from the available experimental outcomes is out of the scopes of the present work, mainly focused on the validation of a numerical fracture framework rather than a specific cohesive constitutive model.

Table 3. Material parameters for the cohesive interfaces.

K_n^0 [N/mm^3]	K_s^0 [N/mm^3]	$\sigma_{\max}$ [MPa]	$\tau_{\max}$ [MPa]	G_{Ic} [N/m]	G_{IIc} [N/m]	α
1.185e6	6.306e5	3.33	3.33	124	124	5

In particular, the initial normal and shear stiffness parameters K_n^0 and K_s^0 have been set to assure, for the given mesh size, no reduction of the Poisson's ratio, according to the condition (37), and a reduction of the Young's modulus of 2%, according to the chart reported in Fig. 7. The corresponding dimensionless stiffness parameters, obtained by graphical linear interpolation, are $\xi = 0.532$ and $\kappa = 104.0$.

For this numerical example, the normal and shear critical stresses, $\sigma_{\max}$ and $\tau_{\max}$, are set equal to each other, as well as the mode-I and mode-II fracture energies. This assumption allows the mesh-induced

strengthening and toughening effects associated with the crack growth in artificial local mixed-mode conditions to be notably reduced.

In this section, a detailed investigation of the toughening effects induced by the mesh has been performed by comparing the present DIM approach, sketched in Fig. 11a with two comparison models. The first comparison model, termed single interface model (SIM) and already used for comparison purposes in [44], is characterized by the presence of cohesive elements arranged along the vertical direction, assuring a collinear propagation of the existing notch (see Fig. 11b). The second comparison model, referred to as controlled diffuse interface model (CDIM), is introduced here for the first time, representing a further aspect of novelty of the present work. Such a model, used in combination with the SIM configuration, is conceived to gain a deeper insight into the reasons for the mesh-induced artificial toughening effects experienced by the DIM approach. In the CDIM approach, a given subset of cohesive interface elements is constrained to lie along the symmetry line of the considered circular region (see Fig. 11c). Such a model is obtained starting from an isotropic Delaunay mesh generated using an additional control edge aligned with the vertical direction, coinciding with the self-similar growth direction for the preexisting crack.

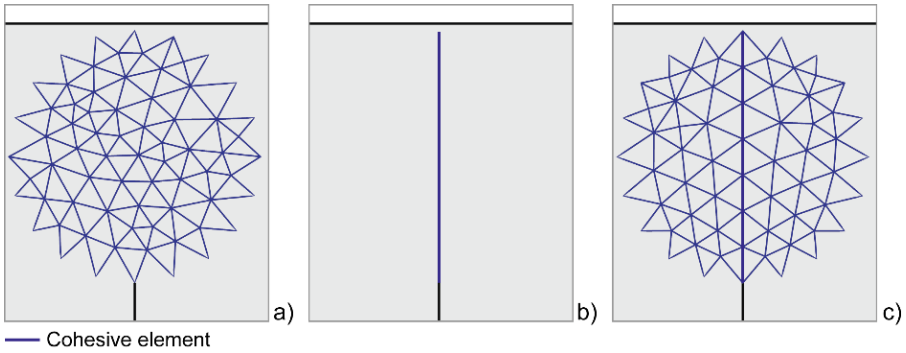

Fig. 11. Cohesive element distribution in three interface models: (a) diffuse interface model (DIM); (b) single interface model (SIM); (c) controlled diffuse interface model (CDIM).

Both SIM and CDIM mesh configurations are characterized by the same average size of the embedded cohesive elements as in the DIM configuration. The resulting Delaunay meshes for the three above-described models, sketched in Fig. 12, are composed of three-node plane stress triangular elements for the bulk and four-node zero-thickness for the cohesive elements. Furthermore, all the meshes include a transition zone to guarantee a graded size variation outside the considered critical region.

The numerical simulations associated with these three models have been performed under quasi-static loading conditions, adopting a Newton-Raphson solution algorithm in combination with a displacement control scheme with increments of 5e-3 mm.

By keeping the SIM configuration as the reference, a comparison between these three models is reported in terms of both load versus mid-span deflection and dissipated fracture energy versus crack mouth opening displacement (CMOD) curves, shown in Fig. 13. The dissipated fracture energy Φ_d has been computed as

the difference between the work of the applied load P and the stored elastic strain energy, both computed at the current displacement δ.

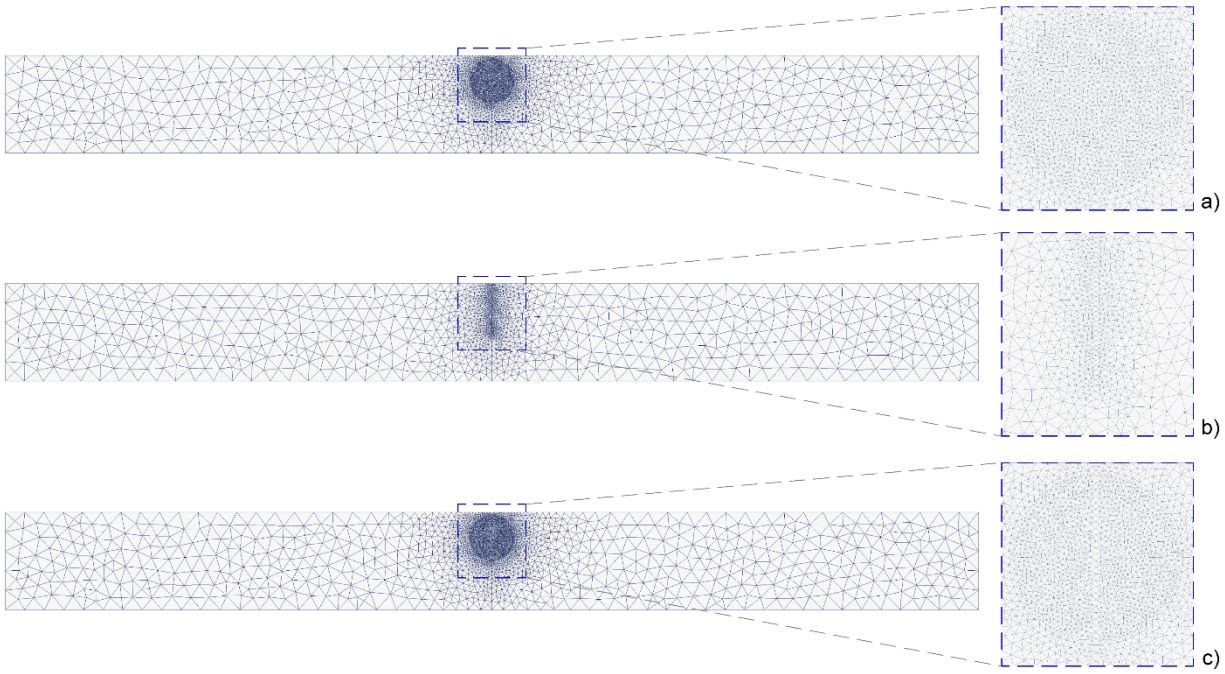

Fig. 12. Delaunay meshes used for the three-point bending test: (a) DIM; (b) SIM; (c) CDIM.

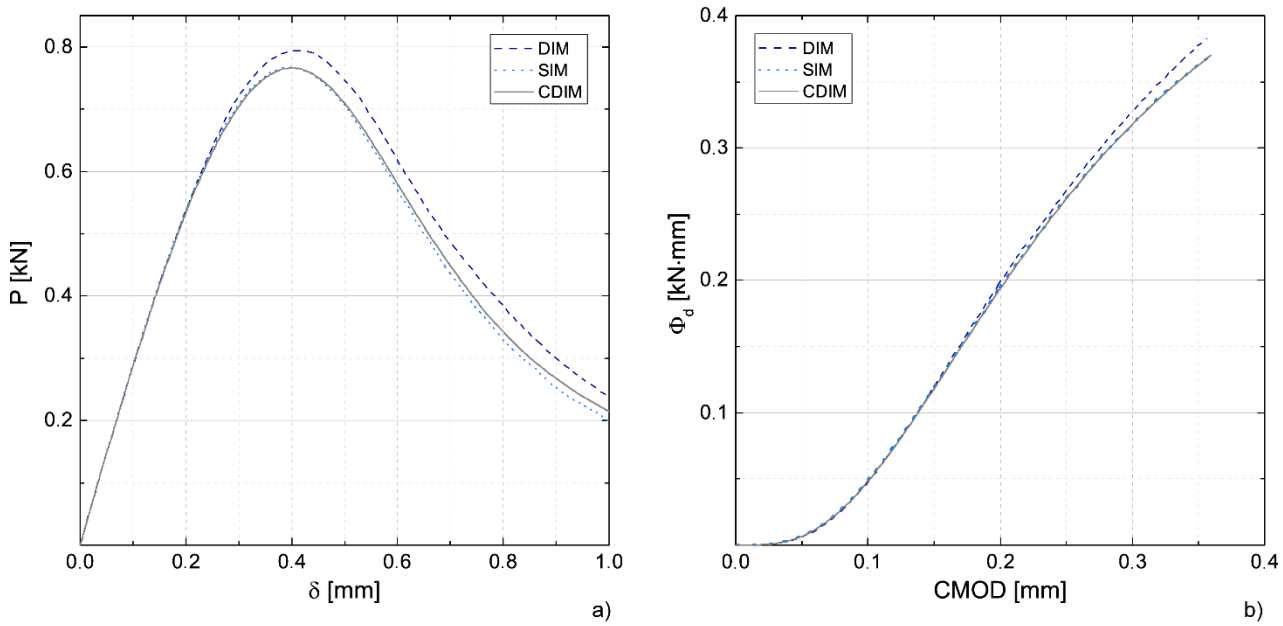

Fig. 13. Comparison between DIM, SIM and CDIM approaches in terms of global structural response: (a) load versus mid-span deflection curve; (b) dissipated fracture energy versus CMOD curve.

Coherently with what has been observed in [44], the DIM approach predicts a slightly stronger structural response, compared to the SIM approach due to the artificial toughening effect induced by the mesh. In particular, as can be deduced from Fig. 13a, the DIM approach leads to a systematic overestimation of the load-carrying capacity predicted by the SIM, at both peak and post-peak regimes, as confirmed by the divergent behaviors of the associated dissipated fracture energy, shown in Fig. 13b. Nevertheless, the peak

load predicted by the DIM approach, of about 0.79 kN, presents a relative error with respect to the reference (i.e. SIM) approach, of only 3.5%, judged to be acceptable for engineering purposes, thus validating the numerical accuracy of the proposed fracture methodology.

The crack path numerically predicted by the DIM approach, shown in Fig. 14a, although forced to lie along the inter-element mesh boundaries, appears to be globally in good accordance with the self-similar crack propagation, taken as the reference one. Moreover, the presence of secondary cracks branching off of the main crack is highlighted.

The second comparison model, i.e. the controlled diffuse interface model (CDIM), has been specifically introduced to understand if the above-mentioned toughening effect is due to the occurrence of secondary cracking or to the jagged path of the main propagating crack. Interestingly, by analyzing again Fig. 13, it can be noted that the global structural response obtained by means of the CDIM approach is practically coincident with that obtained using the reference SIM configuration, in terms of both load versus mid-span deflection and dissipated fracture energy versus CMOD curves.

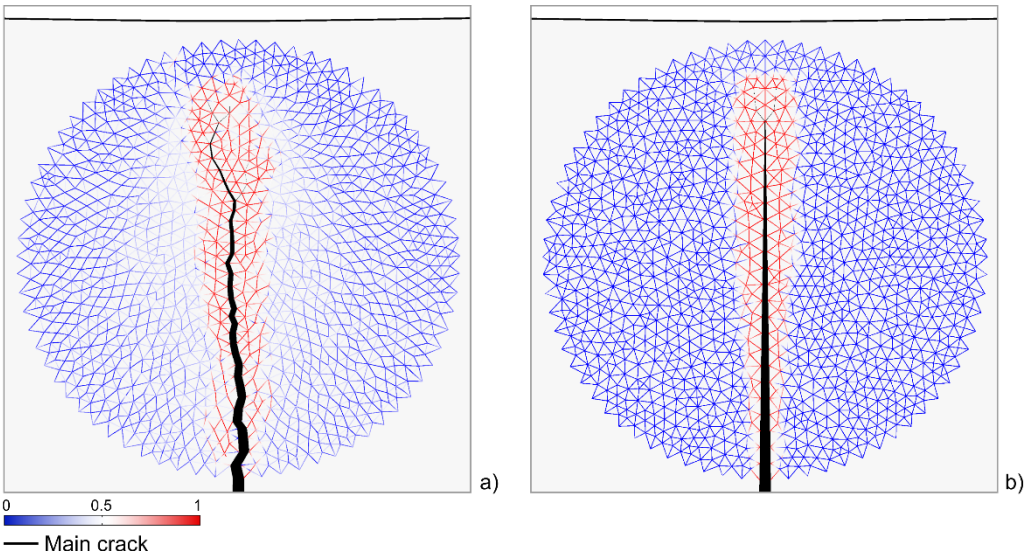

Fig. 14. Main crack path and damage variable map for secondary cracks: (a) DIM; (b) CDIM.

Furthermore, as can be easily observed in Fig. 14b, the main crack path predicted by the CDIM configuration is perfectly aligned with that prescribed by the SIM approach owing to the presence of vertical control edges. However, the appearance of secondary cracks is still experienced, even if localized within a narrower band with respect to the DIM case.

It follows that the nucleation of small secondary cracks in the neighborhood of the main crack tip, as predicted by the present diffuse interface model, has only a negligible influence on the numerically predicted structural behavior, and specifically on the estimated fracture properties. As a consequence, the toughness increase associated with the DIM configuration is not due to the appearance of such secondary cracks, but rather to the tortuosity of the main crack induced by the randomly placed internal boundaries of the adopted unstructured mesh.

More generally, it can be concluded that the simulation of crack localization phenomena in quasi-brittle media, being accompanied by an elastic unloading in the surrounding material, is not sensibly altered by the presence of cohesive elements scattered outside the localization zone. Such a result, rigorously verified for the CDIM configuration (see Fig. 14b), can be likely extended to the DIM approach, provided that the real crack path is well approximated by the mesh boundaries.

5. CONCLUSIONS

In this paper, an enhanced inter-element fracture theoretical model for the nonlinear analysis of quasi-brittle materials subjected to multiple cracking has been proposed, based on a cohesive finite element approach. This model possesses some advantages over most of the existing fracture approaches, since it preserves the discrete nature of cracking phenomena, unlike smeared crack and damage models, and, at the same time, does not require a great implementation effort, unlike X-FEM techniques and other sophisticated intra-element approaches.

The adopted fracture approach, which is a refined version of that introduced by some of the authors in [44], exploits a novel calibration methodology for the elastic parameters of embedded cohesive interfaces, relying on a numerical micromechanical model, aimed at reducing the well-known artificial compliance issues experienced in classical intrinsic approaches.

In the first part of this paper, after that the theoretical formulation is presented, some general results are provided using the proposed calibration methodology. In particular, two charts are obtained for calibrating the normal and tangential elastic stiffness coefficients of the embedded interfaces, as functions of both the Poisson's ratio of the bulk and the admitted reduction in the Young's modulus. These charts are valid for any isotropic and homogeneous material whose nonlinear response can be effectively modeled with any cohesive approach. However, it is worth noting that the proposed cohesive approach could be extended to the case of anisotropic and heterogeneous media in a straightforward manner, without any modification in the general formulation, thus confirming its applicability to a very large class of real-life materials.

In the second part of this paper, the attention has been devoted to the systematic investigation of mesh-induced toughening effects for the adopted fracture approach. Indeed, these effects inevitably lead to an overestimation of the overall structural strength at both peak and post-peak regimes. To this end, a novel comparison model has been introduced, named controlled diffuse interface model, aimed at investigating the capability of the adopted diffuse interface model to predict self-similar crack propagation under pure mode-I loading conditions. The numerical results have demonstrated that, although the well-known lack of crack path convergence is experienced, only a little overestimation of the predicted crack length is found (of about 5%), being strictly related to the mesh-induced tortuosity of the main crack.

Encouraged by the accuracy of the present results concerning the simulation of a single propagating crack, we have proceeded to incorporate the adopted fracture model within a more sophisticated numerical model for studying multiple cracking in plain and reinforced concrete structures. The related results will be presented in the companion Part II paper[56].

ACKNOWLEDGEMENTS

The work of Fabrizio Greco, Paolo Nevone Blasi (University of Calabria) and Sabrina Vantadori (University of Parma) is supported by the Italian Ministry for University and Research (National Research Grant PRIN 2015, No. 2015JW9NJT; Calabria and Parma Research Units).

REFERENCES

1. De Borst R, Remmers JJC, Needleman A, Abellan MA. Discrete vs smeared crack models for concrete fracture: bridging the gap. J Numer Anal Meth Geomech. 2004;28(7-8):583-607.
2. Ingraffea AR. Case studies of simulation of fracture in concrete dams. Eng Fract Mech. 1990;35(1-3):553-564.
3. Piccinin R, Ballarini R, Cattaneo S. Linear elastic fracture mechanics pullout analyses of headed anchors in stressed concrete. J Eng Mech. 2010;136(6):761-768.
4. Bažant ZP. Size effect in blunt fracture: concrete, rock, metal. ASCE J Eng Mech. 1984;110(4):518-535.
5. Elices M, Guinea GV, Gómez J, Planas J. The cohesive zone model: advantages, limitations and challenges. Eng Fract Mech. 2002;69(2):137-163.
6. Camanho PP, Dávila CG, de Moura MF. Numerical simulation of mixed-mode progressive delamination in composite materials. J Compos Mater. 2003;37(16):1415-1438.
7. Turon A, Dávila CG, Camanho PP, Costa J. An engineering solution for mesh size effects in the simulation of delamination using cohesive zone models. Eng Fract Mech. 2007;74(10):1665-1682.
8. Greco F, Lonetti P, Zinno R. An analytical delamination model for laminated plates including bridging effects. Int J Solids Struct. 2002;39(9):2435-2463.
9. Greco F, Lonetti P. Mixed mode dynamic delamination in fiber reinforced composites. Compos Part B-Eng. 2009;40(5):379-392.
10. Bruno D, Greco F, Lonetti P. Dynamic mode I and mode II crack propagation in fiber reinforced composites. Mech Adv Mater Struct. 2009;16(6):442-455.
11. Greco F, Leonetti L, Lonetti P. A novel approach based on ALE and delamination fracture mechanics for multilayered composite beams. Compos Part B-Eng. 2015;78:447-458.

12. Funari MF, Greco F, Lonetti P. A moving interface finite element formulation for layered structures. Compos Part B-Eng. 2016;96:325-337.
13. Bruno D, Greco F, Lo Feudo S, Nevone Blasi P. Multi-layer modeling of edge debonding in strengthened beams using interface stresses and fracture energies. Eng Struct. 2016;109:26-42.
14. Camacho GT, Ortiz M. Computational modelling of impact damage in brittle materials. Int J Solids Struct. 1996;33(20-22):2899-2938.
15. Ooi ET, Yang ZJ, Guo ZY, Dynamic cohesive crack propagation modelling using the scaled boundary finite element method. Fatigue Fract Eng Mater Struct. 2012;35(8):786-800.
16. Kuutti J, Kolari. A local remeshing procedure to simulate crack propagation in quasi-brittle materials. Eng Computation. 2012;29(2):125-143.
17. Sancho JM, Planas J, Cendón DA, Reyes E, Gálvez JC. An embedded crack model for finite element analysis of concrete fracture. Eng Fract Mech. 2007;74(1-2):75-86.
18. Gasser TC, Holzapfel GA. Modeling 3D crack propagation in unreinforced concrete using PUFEM. Comput Methods Appl Mech Eng. 2005;194(25-26):2859-2896.
19. Moës N, Belytschko T. Extended finite element method for cohesive crack growth. Eng Fract Mech. 2002;69(7):813-833.
20. Song JH, Areias PMA, Belytschko T. A method for dynamic crack and shear band propagation with phantom nodes. Int J Numer Methods Eng. 2006;67(6):868-893.
21. Remmers JJC, de Borst R, Needleman A. A cohesive segments method for the simulation of crack growth. Comput Mech. 2003;31(1-2):69-77.
22. Mazars J, Pijaudier-Cabot G. Continuum damage theory – Application to Concrete. J Eng Mech. 1989;115(2):345-365.
23. Oliver J. A consistent Characteristic length for smeared cracking models. Int J Numer Methods Eng. 1989;28(2):461-474.
24. Rots JG. Smeared and discrete representations of localized fracture. Int J Fract. 1991;51(1):45-59.
25. Pijaudier-Cabot G, Bažant Z. Nonlocal damage theory. J Eng Mech. 1987;113(10):1512-1533.
26. Suárez F, Gálvez J, Cendón D. A material model to reproduce mixed-mode fracture in concrete. Fatigue Fract Eng Mater Struct. 2019;42(1):223-238.
27. Červenka J, Červenka V, Laserna S. On crack band model in finite element analysis of concrete fracture in engineering practice. Eng Fract Mech. 2018;197:27-47.
28. Comi C, Perego U. Fracture energy based bi-dissipative damage model for concrete. Int J Solids Struct. 2001;38(36-37):6427-6454.
29. Jirásek M, Patzák B. Consistent tangent stiffness for nonlocal damage models. Comput Struct. 2002;80:1279-1293.

30. Peerlings RHJ, de Borst R, Brekelmans WAM, Geers MGD. Gradient-enhanced damage modelling of concrete fracture. Mech Cohesive-Frict Mater. 1998;3(4):323-342.
31. de Borst R. Simulation of strain localization: a reappraisal of the Cosserat continuum. Eng Computation. 1991;8(4):317-322.
32. Fantuzzi N, Leonetti L, Trovalusci P, Tornabene F. Some novel numerical applications of Cosserat continua. Int J Comput Methods. 2018;15(6):1850054.
33. Matallah M, La Borderie C, Maurel O. A practical method to estimate crack openings in concrete structures. Int J Numer Anal Methods Geomech. 2010;34(15):1615-1633.
34. Ortiz M, Suresh S. Statistical properties of residual stresses and intergranular fracture in ceramic materials. J Appl Mech. 1993;60(1):77-84.
35. Zavattieri PD, Espinosa HD. Grain level analysis of crack initiation and propagation in brittle materials. Acta Mater. 2001;49(20):4291-4311.
36. Maiti S, Rangaswamy K, Geubelle PH. Mesoscale analysis of dynamic fragmentation of ceramics under tension. Acta Mater. 2005;53(3):823-834.
37. Xu XP, Needleman A. Numerical simulations of fast crack growth in brittle solids. J Mech Phys Solids. 1994;42:1397-1434.
38. Papoulia KD, Vavasis SA, Ganguly P. Spatial convergence of crack nucleation using a cohesive finite element model on a pinwheel-based mesh. Int J Numer Methods Eng. 2006;67(1):1-16.
39. Klein PA, Foulk JW, Chen EP, Wimmer SA, Gao HJ. Physics-based modeling of brittle fracture: cohesive formulations and the application of meshfree methods. Theor Appl Fract Mech. 2001;37(1-3):99-166.
40. Espinosa HD, Zavattieri PD. A grain level model for the study of failure initiation and evolution in polycrystalline brittle materials. Part I: Theory and numerical implementation. Mech Mater. 2003;35(3-6):333-364.
41. Tomar V, Zhai J, Zhou M. Bounds for element size in a variable stiffness cohesive finite element model. Int J Numer Methods Eng. 2004;61(11):1894-1920.
42. de Borst R, Remmers JJC, Needleman A. Mesh-independent discrete numerical representations of cohesive-zone models. Eng Fract Mech. 2006;73(2):160-177.
43. Blal N, Daridon L, Monerie Y, Pagano S. Artificial compliance inherent to the intrinsic cohesive zone models: criteria and application to planar meshes. Int J Fract. 2012;178(1-2):71-83.
44. De Maio U, Fabbrocino F, Greco F, Leonetti L, Lonetti P. A study of concrete cover separation failure in FRP-plated RC beams via an inter-element fracture approach. Compos Struct. 2019;212:625-636.
45. Mori T, Tanaka K. Average stress in matrix and average elastic energy of materials with misfitting inclusions. Acta Metall. 1973;21:571-574.

46. Hassani B, Hinton E. A review of homogenization and topology optimization I – homogenization theory for media with periodic structure. Comput Struct. 1998;69:707-717.
47. Hori M, Nemat-Nasser S. On two micromechanics theories for determining micro–macro relations in heterogeneous solids. Mech Mater. 1999;31:667-682.
48. Ghosh S, Lee K, Moorthy S. Two scale analysis of heterogeneous elastic-plastic materials with asymptotic homogenization and Voronoi cell finite element model. Comput Methods Appl Mech Eng. 1996;132:63-116.
49. Ostoja-Starzewski M. Material spatial randomness: From statistical to representative volume element. Probabilist Eng Mech. 2006;21:112-132.
50. Gusella F, Cluni F, Gusella V. Homogenization of dynamic behaviour of heterogeneous beams with random Young's modulus. Eur J Mech A-Solid. 2019;73:260-267.
51. Gusella F, Cluni F, Gusella V. Homogenization of the heterogeneous beam dynamics: The influence of the random Young's modulus mixing law. Compos Part B-Eng. 2019;167:608-614.
52. Li S, Wang G, Morgan E. Effective elastic moduli of two dimensional solids with distributed cohesive microcracks. Eur J Mech A Solids. 2004;23(6):925-933.
53. Bruno D, Greco F, Lonetti P, Nevone Blasi P. Influence of micro-cracking and contact on the effective properties of composite materials. Simul Model Pract Theor. 2008;16(8):861-884.
54. Moakher M, Norris AN. The closest elastic tensor of arbitrary symmetry to an elasticity tensor of lower symmetry. J Elasticity. 2006;85(3):215-263.
55. Comsol AB. Comsol Multiphysics Reference Manual. 2018.
56. De Maio U, Greco F, Leonetti L, Luciano R, Nevone Blasi P, Vantadori S. A refined diffuse cohesive approach for the failure analysis in quasi-brittle materials – Part II: application to plain and reinforced concrete structures. Fatigue Fract Eng Mater Struct. (Submitted)
57. Kanit T, Forest S, Galliet I, Mounoury V, Jeulin D. Determination of the size of the representative volume element for random composites: statistical and numerical approach. Int J Solids Struct. 2003;40(13-14):3647-3679.
58. Petersson PE. Crack growth and development of fracture zones in plain concrete and similar materials. Rep. TVBM-1006, Division of Building Materials, Lund Institute of Technology, Lund, Sweden. 1981.
59. Fathy AM, Sanz B, Sancho JM, Planas J. Determination of the bilinear stress-crack opening curve for normal- and high-strength concrete. Fatigue Fract Eng Mater Struct. 2008;31(7):539-548.
60. Shanmugam V, Penmetsa R, Tuegel E. Calibration of a probabilistic cohesive zone model for generating a fracture nomograph. Fatigue Fract Eng Mater Struct. 2012;35(4):328-346.